

Taylor vortices in yield stress fluids with static wall layers on the outer cylinder

S. Topayev¹, C. Nouar^{2,†} and I. Frigaard³

¹Zhetysu University named after I. Zhansugurov, 187a Zhansugurova street, 040009 Taldykorgan, Kazakhstan

²LEMTA, UMR 7563, CNRS – Université de Lorraine, 2 Avenue de la Forêt de Haye, BP 90161, 54505 Vandoeuvre Lès Nancy, France

³Department of Mathematics, University of British Columbia, 1984 Mathematics Road, Vancouver, BC V6T 1Z4, Canada

(Received 26 March 2023; revised 28 August 2023; accepted 10 October 2023)

A linear stability analysis of circular Couette flow of a Bingham fluid subjected to axisymmetric perturbations was presented by Peng & Zhu (*J. Fluid Mech.*, vol. 512, 2004, pp. 21–45) and Landry *et al.* (*J. Fluid Mech.*, vol. 560, 2006, pp. 321–353). Here, we consider the stability of this flow with respect to a finite amplitude perturbation. We focus particularly on the case where the basic flow has an unyielded fluid layer on outer cylinder. A weakly nonlinear stability analysis is developed for a wide gap and a narrow gap. A third-order Ginzburg–Landau equation is derived, and the influence of the different nonlinearities on bifurcation features is investigated in detail. The results indicate that: (i) the nonlinear inertial terms act in favour of pitchfork supercritical bifurcation and the nonlinear yield stress terms promote a subcritical bifurcation; (ii) for a range of Bingham numbers B , the extent of which depends on the radius ratio and outer Reynolds number, the nonlinear yield stress terms are dominant and the primary bifurcation is subcritical. The amplitude analysis indicates that in the supercritical bifurcation regime, near the threshold, when the nonlinear inertial terms are dominant, the amplitude decreases slightly with increasing B . Once the nonlinear yield stress terms start to become significant, the equilibrium amplitude increases substantially with increasing B . Similar trends are observed for Taylor vortex strength. Finally, the erosion of the static layer is analysed. It is shown that the nonlinear yield stress terms play a significant role.

Key words: nonlinear instability, Taylor–Couette flow

† Email address for correspondence: cherif.nouar@univ-lorraine.fr

1. Introduction

Viscoplastic material behaves as a ‘solid’ from a kinematic point of view when the applied stress is below a threshold value $\hat{\tau}_y$, and flows like a viscous fluid for stresses higher than $\hat{\tau}_y$. The solid-like behaviour is associated with elasticity, whereby the continuum deforms when subjected to a given stress and there is a complete strain recovery when the forcing is removed. In general, the critical strain before yielding is small (Coussot 1999), and the elastic properties may be neglected reasonably when the stress is below $\hat{\tau}_y$.

In the present work, we follow this assumption. Many materials exhibit a yield stress (Bird, Daii & Yarusso 1983), such as in drilling mud in the oil industry, and in cement, paints, cosmetics and pharmaceutical preparations, as well as a large variety of food products. Although many models have been proposed to describe the behaviour of such materials, e.g. the Herschel–Bulkley, Casson or Robertson–Stiff models (see Agwu *et al.* 2021), the Bingham model is the most well known and simple. Furthermore, it contains all the ingredients of viscoplastic materials, namely a yield stress and a nonlinear variation of the effective viscosity with the shear rate. In this model, the material is considered to be rigid below a yield criterion described by the von Mises criterion, and is nonlinearly viscous above the yield criterion. The determination of these two regions is not a trivial task, especially in two- and three-dimensional flows. A review on yield stress fluids can be found in Balmforth, Frigaard & Ovarlez (2014), Bonn *et al.* (2017) and Coussot (2017). Although they are commonly used as industrial fluids, there are surprisingly few published works that focus on the stability of yield stress fluid flows.

In the present work, we consider the stability of circular Couette flow for a Bingham fluid. The first linear stability analysis was done by Graebel (1961) using a narrow gap approximation. He found that the yield stress has a stabilizing effect. This problem was later reconsidered by Peng & Zhu (2004) assuming axisymmetric disturbances. The most interesting feature of the results is the non-monotonicity of the critical inner cylinder Reynolds number Re_{1c} for wide gap co-rotating cylinders as the Bingham number is increased. It is the only study that we know of where a yield stress fluid is less stable than the corresponding Newtonian fluid flow. It is explained by Landry, Frigaard & Martinez (2006) that in co-rotating cylinders (at small B), the decrease of the critical Reynolds number is due to an increase of strain rate of the basic flow, which amplifies the production term in the linear energy equation. The production term provides the only means by which energy is exchanged between the base flow and the perturbation. This linear analysis is completed with the transient growth characteristics of both axisymmetric and non-axisymmetric perturbations (Agbessi *et al.* 2015; Chen, Wan & Zhang 2015). It is shown in particular that the yield stress reduces strongly the transient growth.

A numerical simulation of axisymmetric Taylor–Couette flow of Bingham fluids was performed by Jeng & Zhu (2010), in the case of a wide gap with a radius ratio $\eta = R_1/R_2 = 0.5$. To overcome the discontinuity in the Bingham model, in the transition from solid-like to liquid-like, Papanastasiou regularization (Papanastasiou 1987) is used, which treats the whole material domain as a fluid of variable viscosity, and locally assigns a large but finite value of viscosity to the unyielded region. A review of popular regularization models has been carried out by Frigaard & Nouar (2005).

When the outer cylinder is at rest, and for a fixed inner cylinder Reynolds number Re_1 (not for a fixed relative distance to the onset of vortices, $\epsilon = (Re_1 - Re_{1c})/Re_{1c}$), Jeng & Zhu (2010) found that the intensity of the vortex flow is weaker than that obtained for a Newtonian fluid. For the co-rotation situation with fixed outer and inner Reynolds

numbers, the authors found that the intensity of the vortex flow is initially strengthened with increasing the yield stress, and then weakened as the yield stress is raised further.

Experimental results are sparse. Using Carbopol solution as a model fluid, Naimi, Devienne & Lebouché (1990) observed axisymmetric Taylor vortices. It is indicated that the yield stress has a stabilizing effect. Actually, the focus of this study was on heat transfer rather than on hydrodynamic stability.

A natural sequel to the linear theory developed by Peng & Zhu (2004) and Landry *et al.* (2006) is to consider the stability of a circular Couette flow of a Bingham fluid with respect to a finite-amplitude perturbation. In this case, nonlinear effects can no longer be neglected, and the linear framework used previously becomes inapplicable. In yield stress fluids equations of motion, in addition to the quadratic nonlinearity of the inertial terms, we also have a nonlinearity in the rheological law. In the research of nonlinear phenomena, much attention has been devoted to the weakly nonlinear phase around criticality, as analytical modelling of the weak nonlinearity is possible. A multiple scale expansion method is generally applied for the study of weak nonlinearity. This mathematical tool is employed in the present work. Alternatively, one can use the amplitude expansion method surveyed by Herbert (1983), or the centre manifold reduction (Fujimura 1991). Fujimura (1989, 1991) demonstrated that these theoretical tools are equivalent in the derivation of the Ginzburg–Landau equation that models the temporal evolution of the disturbance amplitude. This equation allows us to determine whether the nonlinearities saturate the linear instability, and at what value of the disturbance amplitude. For a Newtonian Taylor–Couette flow with fixed outer cylinder, the primary bifurcation is supercritical, i.e. the nonlinear inertial terms saturate the amplitude of the vortices. Using the amplitude expansion method, Davey (1962) investigated the structure of the supercritical Taylor vortex flow. It is shown that the distortion of the mean azimuthal velocity profile by the Reynolds stress plays a significant role in the saturation process. For a purely viscous shear-thinning fluid described, for example by the Carreau model, Topayev *et al.* (2019) showed that the nonlinearity of the rheological model tends to accelerate the mean flow in the annular space due to the reduction of the viscous dissipation induced by the viscosity perturbation (see also Chekila *et al.* (2011) for another configuration). This reduction in the viscous dissipation is modest and does not alter the supercritical nature of the primary bifurcation, i.e. the nonlinear inertial terms remain dominant. This is perhaps not surprising as at sufficiently high shear rate, the viscosity perturbation due to a shear rate disturbance is very weak. In the case of a Bingham fluid with the presence of a static layer attached to the outer cylinder, the reduction of the viscous dissipation can be more substantial due to the strong nonlinear increase of the viscosity near the yield surface. The role of nonlinear yield stress terms may become sufficiently important comparatively to the nonlinear inertial terms to change the nature of the bifurcation.

The objective is to investigate the first effects of nonlinear yield stress terms on the nature of the primary bifurcation, the intensity of vortex flow and the erosion of the static layer. An approach based on weakly nonlinear analysis with a multiple scales method is adopted. Very few people have carried out a weakly nonlinear analysis for these yield stress fluid models. To the best of our knowledge, there is only the work of Metivier *et al.* (2010) dealing with plane Poiseuille–Rayleigh–Bénard flow of a Bingham fluid.

The results of this study could have applications in Couette rheometry, especially with a wide gap (Ovarlez *et al.* 2008). They can also be considered as a first step in the study of rotating filtration systems involving yield stress fluids (Martinand, Serre & Lueptow 2017).

This paper is organized as follows. In § 2, we formulate the physical problem, state the governing equations and define the dimensionless parameters. The velocity and

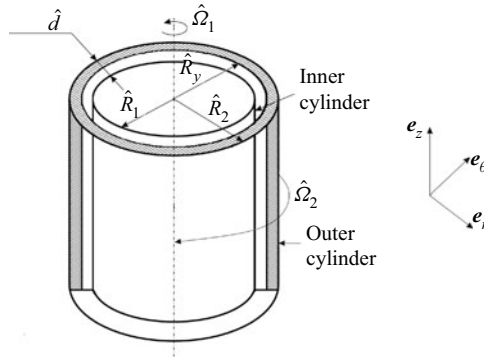


Figure 1. Geometry sketch and parameters of the Couette flow of a yield stress fluid with a plug zone represented by the dashed area. The yield surface radius \hat{R}_y is defined by (2.15).

viscosity profiles of the base state are discussed, and the disturbance equations are derived. Subsequently, the linearization of the disturbance equations and the eigenvalue problem derivation for the linear stability analysis are presented in § 3. In § 4, the weakly nonlinear scheme based on a multiple scales method is described in detail, as well as the method to derive the Ginzburg–Landau equation and to obtain the first Landau constant. We focus mainly on the situation where a static layer is attached to the outer wall. In § 5, we present and discuss the numerical results dealing with the influence of the Bingham number on the nature of primary bifurcation and the flow structure. Finally, in § 6, the relevant results of the present study are summarized.

2. Problem formulation

We consider the flow between two infinitely long concentric cylinders (see figure 1), with inner and outer radii \hat{R}_1 and \hat{R}_2 , that rotate independently with angular speeds $\hat{\Omega}_1$ (inner) and $\hat{\Omega}_2$ (outer). The scaled momentum and mass conservation equations are

$$\partial_t \mathbf{U} + Re_1 (\nabla \mathbf{U}) \cdot \mathbf{U} = -\nabla P + \nabla \cdot \boldsymbol{\tau}, \tag{2.1}$$

$$\nabla \cdot \mathbf{U} = 0, \tag{2.2}$$

where \mathbf{U} is the velocity, P is the pressure, $\boldsymbol{\tau}$ is the deviatoric stress tensor, and Re_1 is the inner cylinder Reynolds number:

$$Re_1 = \frac{\hat{\rho} \hat{R}_1 \hat{\Omega}_1 \hat{d}}{\hat{\mu}_p}. \tag{2.3}$$

Here, $\hat{\rho}$ and $\hat{\mu}_p$ are the density and the plastic viscosity. The velocity vector is of the form $\mathbf{U} = U\mathbf{e}_r + V\mathbf{e}_\theta + W\mathbf{e}_z$, where U, V, W are the velocity components, and $\mathbf{e}_r, \mathbf{e}_\theta, \mathbf{e}_z$ are unit vectors in the radial (r), azimuthal (θ) and axial (z) directions. Lengths are scaled with the annular gap $\hat{d} = \hat{R}_2 - \hat{R}_1$. The velocities are scaled with $\hat{\Omega}_1 \hat{R}_1$ (velocity of the inner cylinder). The time is scaled with the viscous diffusion time $\hat{\rho} \hat{d}^2 / \hat{\mu}_p$. The pressure and stresses are scaled with $\hat{\mu}_p \hat{R}_1 \hat{\Omega}_1 / \hat{d}$. By convention, we take $\hat{\Omega}_1 > 0$.

Using the von Mises yield criterion, the dimensionless constitutive equations for Bingham fluids are

$$\tau_{ij} = \left(1 + \frac{B}{\dot{\gamma}}\right) \dot{\gamma}_{ij} \iff \tau > B, \quad (2.4)$$

$$\dot{\gamma} = 0 \iff \tau \leq B, \quad (2.5)$$

where $\dot{\gamma} = \sqrt{\dot{\gamma}_{ij}\dot{\gamma}_{ij}/2}$ and $\tau = \sqrt{\tau_{ij}\tau_{ij}/2}$ are the second invariant of the strain rate $\dot{\boldsymbol{\gamma}}$ and deviatoric stress $\boldsymbol{\tau}$ tensors, respectively. The components of $\dot{\boldsymbol{\gamma}}$ are $\dot{\gamma}_{ij} = U_{ij} + U_{ji}$. The Bingham number B is defined as

$$B = \frac{\hat{\tau}_y \hat{d}}{\hat{\mu}_p \hat{R}_1 \hat{\Omega}_1}, \quad (2.6)$$

which represents the ratio of the yield stress $\hat{\tau}_y$ to a nominal viscous stress $\hat{\mu}_p \hat{R}_1 \hat{\Omega}_1 / \hat{d}$. In the regions where the yield stress is not exceeded, the rate of strain tensor is identically zero (i.e. no local deformation occurs) and the stress tensor is undetermined. The fluid within these regions is constrained to move as a rigid body and hereafter will be referred to as the ‘plug zone’. In contact with a quiescent wall, the plug zone remains static.

Two further dimensionless parameters will be used: the outer Reynolds number Re_2 and the radius ratio η ,

$$Re_2 = \frac{\hat{\rho} \hat{R}_2 \hat{\Omega}_2 \hat{d}}{\hat{\mu}_p}, \quad \eta = \frac{\hat{R}_1}{\hat{R}_2}. \quad (2.7a,b)$$

Remark. Peng & Zhu (2004) used the Hedström number (Hedström 1952; Hanks 1967) $He = \hat{\rho} \hat{d}^2 \hat{\tau}_y / \hat{\mu}_p^2 = B Re_1$ rather than the Bingham number. It can be interpreted as the ratio of the yield stress $\hat{\tau}_y$ to a viscous stress $\hat{\mu}_p \hat{v}_d / \hat{d}$, where \hat{v}_d is the viscous diffusion velocity scale. Following Landry *et al.* (2006), the choice of B rather than He in the present work is driven by two considerations. First, as will be shown in the next subsection, the basic Couette flows depends solely on B , η and Re_2/Re_1 . Second, in using He , large values of He may correspond to modest values of B , leading to relatively small changes in the Couette flow. Finally, the use of either He or B can be considered as simply a matter of choice.

2.1. Basic flow

The base Couette flow velocity $\mathbf{U}_b = (0, V_b(r), 0)$ is derived from

$$0 = \frac{1}{r^2} \frac{d}{dr} \left(r^2 \tau_{r\theta} \right), \quad r \in \left[\frac{\eta}{1-\eta}, \frac{1}{1-\eta} \right], \quad (2.8)$$

$$\tau_{r\theta} = \left[1 + \frac{B}{|\dot{\gamma}_{r\theta}|} \right] \dot{\gamma}_{r\theta} \iff |\tau_{r\theta}| > B, \quad (2.9)$$

$$|\dot{\gamma}_{r\theta}| = 0 \iff |\tau_{r\theta}| \leq B, \quad (2.10)$$

$$\dot{\gamma}_{r\theta} = \frac{dV_b}{dr} - \frac{V_b}{r}, \quad (2.11)$$

with boundary conditions

$$V_b = 1 \quad \text{at } r = R_1 = \frac{\eta}{1 - \eta}, \tag{2.12}$$

$$V_b = \frac{Re_2}{Re_1} \quad \text{at } r = R_2 = \frac{1}{1 - \eta}. \tag{2.13}$$

The basic flow equations are determined fully by the set of parameters B , η and Re_2/Re_1 .

From (2.8), we have

$$\tau_{r\theta} = \frac{\tau_i \eta^2}{r^2(1 - \eta)^2}, \quad \text{where } \tau_i = \tau_{r\theta}(r = R_1). \tag{2.14}$$

Therefore, $\tau_{r\theta}$ does not change sign in the annulus, and $|\tau_{r\theta}|$ decreases with r . Consequently, if there is an unyielded plug zone in the annulus, then it must be bounded inside by a yield surface, say at $r = R_y$, and must extend to the outer wall. The position of R_y is defined by $|\tau_{r\theta}| = B$:

$$R_y = \frac{\eta}{1 - \eta} \sqrt{\frac{|\tau_i|}{B}}. \tag{2.15}$$

The base solutions are of three types: (i) the inner and outer cylinders rotate with the same angular velocity, the fluid is fully unyielded in the annular gap; (ii) there may be a layer of unyielded fluid attached to the outer wall; (iii) the fluid may be fully yielded through the annular gap. The regions where the three solutions may be found can be visualized in the plane (Re_1, Re_2) . Fully unyielded flows are found along the line

$$Re_1 = \eta Re_2. \tag{2.16}$$

Partially yielded flows are found in the domains bounded by the above line and the lines

$$\frac{Re_2}{Re_1} = \frac{1}{\eta} \pm Bf(\eta), \tag{2.17}$$

where $f(\eta)$ is defined by (Landry *et al.* 2006)

$$f(\eta) = \frac{1 + \eta}{2\eta^2} - \frac{\ln(1/\eta)}{1 - \eta}. \tag{2.18}$$

As an example, figure 2 shows the domains where the three solutions hold in the plane (Re_2, Re_1) in the case of a narrow gap $\eta = 0.883$ and a wide gap $\eta = 0.4$. The Bingham number is fixed at $B = 5$. In domains of the plane (Re_2, Re_1) where the fluid is fully yielded or partially yielded, the velocity profile $V_b(r)$ is given by

$$V_b(r) = \begin{cases} \frac{Re_2}{Re_1} \frac{r}{R_2} + \frac{\tau_i R_1^2}{2} r \left[\frac{1}{R_0^2} - \frac{1}{r^2} \right] + Br \ln \left(\frac{R_0}{r} \right) \text{sgn}(\tau_i), & R_1 \leq r \leq R_0, \\ \frac{Re_2}{Re_1} \frac{r}{R_2}, & R_0 \leq r \leq R_2, \end{cases} \tag{2.19}$$

where $R_0 = \min(R_y, R_2)$. An illustration of basic velocity profiles $V_b(r)$ at different values of B in the case of co-rotating ($Re_1 = 1000$, $Re_2 = 100$) and counter-rotating ($Re_1 = 1000$, $Re_2 = -100$) cylinders for a narrow gap and a wide gap is given by figure 3.

Taylor vortices in yield stress fluids

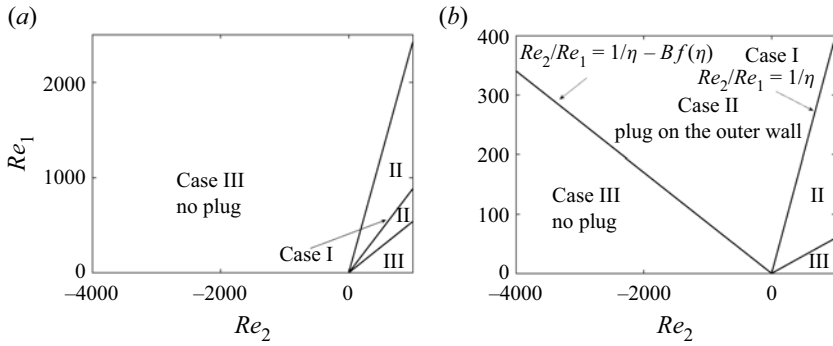


Figure 2. Flow regimes in the plane (Re_2, Re_1) at $B = 5$: (a) narrow gap $\eta = 0.883$, and (b) wide gap $\eta = 0.4$.

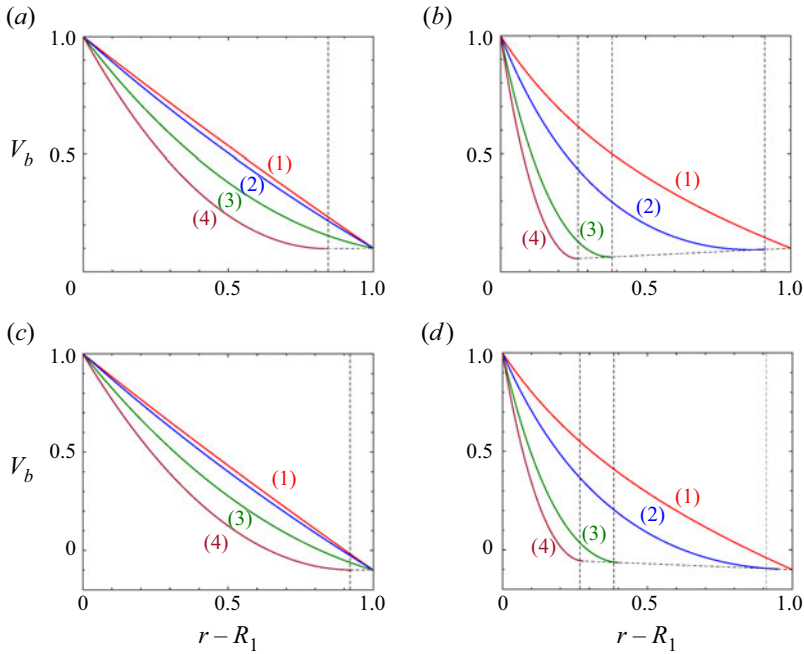


Figure 3. Basic velocity profiles $V_b(r)$. Case of co-rotating cylinders with $Re_2 = 100$ and $Re_1 = 1000$: (a) $\eta = 0.883$, and (b) $\eta = 0.4$. Case of counter-rotating cylinders with $Re_2 = -100$ and $Re_1 = 1000$: (c) $\eta = 0.883$, and (d) $\eta = 0.4$. Curves are (1) $B = 0$, (2) $B = 1$, (3) $B = 5$, and (4) $B = 10$.

The position R_y of the yield surface is indicated by a vertical dashed line. In the static layer ($R_y \leq r \leq R_2$), V_b varies linearly with r . The nonlinear variation of the effective viscosity $\mu = 1 + B/\dot{\gamma}$ in the yielded zone is shown in figure 4. According to the Bingham model, μ increases from the inner wall and tends to infinity near the yield surface. The degree of nonlinearity of the rheological behaviour becomes stronger with increasing B .

Remarks.

- (i) It can be shown straightforwardly that there is a similarity mapping that maps the basic solution II onto a basic solution III with an outer radius equal to the

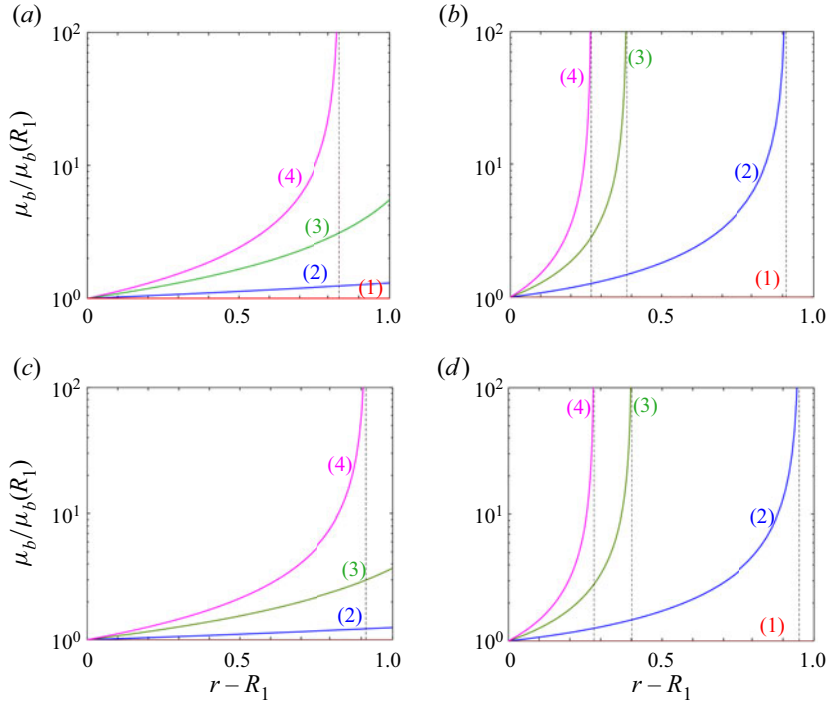


Figure 4. Basic viscosity profiles $\mu_b(r)$. Case of co-rotating cylinders with $Re_2 = 100$ and $Re_1 = 1000$: (a) $\eta = 0.883$, and (b) $\eta = 0.4$. Case of counter-rotating cylinders with $Re_2 = -100$ and $Re_1 = 1000$: (c) $\eta = 0.883$, and (d) $\eta = 0.4$. Curves are (1) $B = 0$, (2) $B = 1$, (3) $B = 5$, and (4) $B = 10$.

yield surface radius. Mapping of the basic solution II consists simply on rescaling the length, by substituting $r = \tilde{r}(R_0 - R_1)$ with $\tilde{\eta}/(1 - \tilde{\eta}) \leq \tilde{r} \leq 1/(1 - \tilde{\eta})$, where $\tilde{\eta} = R_1/R_0$ (Landry *et al.* 2006). This leads to the scalings $\tilde{B} = B(R_0 - R_1)$, $\tilde{\tau}_i = \tau_i(R_0 - R_1)$ and $\tilde{Re}_2/\tilde{Re}_1 = (Re_2/Re_1)((1 - \tilde{\eta})/R_2)$.

- (ii) The terms ‘narrow gap’ and ‘wide gap’ are, of course, related to the radius ratio (Chandrasekhar 1958, 2013; Donnelly 1958; Razzak, Khoo & Lua 2019). In the narrow gap problems, the annular gap is much smaller than the mean radius and usually indicates that the radius ratio is $\eta > 0.5$. For the wide gap problems, $\eta \leq 0.5$. From a physical point of view, the critical Reynolds number Re_c at which Taylor vortices appear increases with increase in radius ratio in narrow gap problems, while the opposite behaviour is observed for wide gap problems.

2.2. Perturbation equations

A perturbation of a small amplitude (\mathbf{u}, p) is imposed on the basic flow (U_b, P_b) . The perturbed flow is then given by

$$(U_b + \mathbf{u}, P_b + p) = (u, V_b + v, w, P_b + p). \tag{2.20}$$

The perturbation equations in the yielded parts of the flow are derived straightforwardly:

$$\nabla \cdot \mathbf{u} = 0, \tag{2.21}$$

$$\frac{\partial \mathbf{u}}{\partial t} = \mathbf{L}(\mathbf{u}, p) + \mathbf{N}(\mathbf{u}). \tag{2.22}$$

The operator $\mathbf{L}(\mathbf{u}, p)$ denotes the linear part of the perturbation equations, which consists of four parts:

$$\mathbf{L}(\mathbf{u}, p) = Re_1 \mathbf{LI}(\mathbf{u}) - \nabla p + \mathbf{LV}(\mathbf{u}) + \mathbf{BLY}(\mathbf{u}), \tag{2.23}$$

describing inertial, pressure, viscous and yield stress effects. The inertial, pressure and viscous operators are identical to those for a Newtonian fluid:

$$\mathbf{LI}(\mathbf{u}) = -[(\mathbf{U}_b \cdot \nabla)\mathbf{u} + (\mathbf{u} \cdot \nabla)\mathbf{U}_b], \tag{2.24}$$

$$\mathbf{LV}(\mathbf{u}) = \nabla \cdot \dot{\boldsymbol{\gamma}}. \tag{2.25}$$

The yield stress term is addressed below along with the nonlinear parts. The terms in \mathbf{N} are significant for nonlinear perturbations. This includes the contribution from the inertial terms and from perturbations of the shear stress tensor, where only the yield stress contributions are nonlinear. This can be written as

$$\mathbf{N}(\mathbf{u}) = Re_1 \mathbf{NI}(\mathbf{u}) + \mathbf{BNY}(\mathbf{u}), \tag{2.26}$$

where the inertial operator $\mathbf{NI}(\mathbf{u})$ reads

$$\mathbf{NI}(\mathbf{u}) = -(\mathbf{u} \cdot \nabla)\mathbf{u}. \tag{2.27}$$

2.3. Yield stress terms

The components of the shear stress tensor can be written as

$$\tau_{ij} = \dot{\gamma}_{ij} + \mathbf{B}M_{ij}. \tag{2.28}$$

In a part of the fluid where the yield stress is not exceeded, the τ_{ij} are indeterminate. Conversely, in a part of the fluid where the yield stress is exceeded, the M_{ij} are given by

$$M_{ij} = \frac{\dot{\gamma}_{ij}}{\dot{\gamma}}. \tag{2.29}$$

The contributions to the yield stress in the perturbation equations all come from the expressions $M_{ij}(\mathbf{U}_b + \mathbf{u}) - M_{ij}(\mathbf{U}_b)$, which, for small finite \mathbf{u} , can be found by expanding about the base flow in a Taylor series:

$$M_{ij}(\mathbf{U}_b + \mathbf{u}) - M_{ij}(\mathbf{U}_b) = m_{1,ij}(\mathbf{u}) + m_{2,ij}(\mathbf{u}, \mathbf{u}) + m_{3,ij}(\mathbf{u}, \mathbf{u}, \mathbf{u}) + \dots \tag{2.30}$$

The terms in $m_{k,ij}$ contain products of k components of \mathbf{u} . For $k = 1, 2, 3$, the general expressions of $m_{k,ij}$ are provided in §1 of the supplementary material available at <https://doi.org/10.1017/jfm.2023.874>. For the specific base flow that we have, where only $\dot{\gamma}_{r\theta}(\mathbf{U}_b) = \dot{\gamma}_{\theta r}(\mathbf{U}_b) \neq 0$, some simplifications are made:

$$m_{1,ij} = 0, \quad ij = r\theta, \theta r, \tag{2.31}$$

$$m_{1,ij} = \frac{\dot{\gamma}_{ij}(\mathbf{u})}{\dot{\gamma}(\mathbf{U}_b)}, \quad ij \neq r\theta, \theta r, \tag{2.32}$$

$$m_{2,ij} = \frac{\text{sgn}(\dot{\gamma}_{r\theta}(\mathbf{U}_b))}{2\dot{\gamma}^2(\mathbf{U}_b)} \left[\dot{\gamma}_{r\theta}^2(\mathbf{u}) - \dot{\gamma}^2(\mathbf{u}) \right], \quad ij = r\theta, \theta r, \tag{2.33}$$

$$m_{2,ij} = -\frac{\text{sgn}(\dot{\gamma}_{r\theta}(\mathbf{U}_b))}{\dot{\gamma}^2(\mathbf{U}_b)} \dot{\gamma}_{ij}(\mathbf{u}) \dot{\gamma}_{r\theta}(\mathbf{u}), \quad ij \neq r\theta, \theta r, \tag{2.34}$$

$$m_{3,ij} = \frac{\dot{\gamma}_{r\theta}(\mathbf{u})}{[\dot{\gamma}(\mathbf{U}_b)]^3} \left[\dot{\gamma}^2(\mathbf{u}) - \dot{\gamma}_{r\theta}^2(\mathbf{u}) \right], \quad ij = r\theta, \theta r, \tag{2.35}$$

$$m_{3,ij} = \frac{1}{2[\dot{\gamma}(\mathbf{U}_b)]^3} \left[\frac{3}{2} \dot{\gamma}_{r\theta}^2(\mathbf{u}) - \dot{\gamma}^2(\mathbf{u}) \right] \dot{\gamma}_{ij}(\mathbf{u}), \quad ij \neq r\theta, \theta r. \tag{2.36}$$

In terms of $m_{k,ij}, k = 1, 2, 3$, we may now define the linear ($k = 1$) and nonlinear ($k = 2, 3$) Bingham perturbation terms as

$$\mathbf{LY} = \nabla \cdot \mathbf{m}_1 \quad \text{and} \quad \mathbf{NY}_k = \nabla \cdot \mathbf{m}_k. \tag{2.37a,b}$$

3. Linear stability analysis

The basic flow is supposed to be perturbed by an infinitesimal disturbance. The linearized perturbation equations can be written formally as

$$\nabla \cdot \mathbf{u} = 0, \tag{3.1}$$

$$\frac{\partial \mathbf{u}}{\partial t} = -\nabla p + Re_1 \mathbf{LI}(\mathbf{u}) + \mathbf{LV}(\mathbf{u}) + \mathbf{BLY}(\mathbf{u}). \tag{3.2}$$

3.1. Boundary conditions

If the fluid is fully yielded in all the annular space (case III in figure 2), then the no-slip conditions at both walls are imposed:

$$\mathbf{u} = 0 \quad \text{at } r = R_1, \tag{3.3}$$

$$\mathbf{u} = 0 \quad \text{at } r = R_2. \tag{3.4}$$

If the fluid is partially yielded (case II of the base solutions), then in the region where the yield stress is exceeded, the components of the deviatoric stress tensor are assumed linearly perturbed and $M_{ij}(\mathbf{U}_b + \mathbf{u}) - M_{ij}(\mathbf{U}_b) = m_{1,ij}(\mathbf{u})$. Therefore, it can be assumed that the yield surface will be also linearly perturbed from its initial position R_y :

$$r = R_y + h, \quad \text{with } h \ll R_2 - R_y. \tag{3.5}$$

In other words, it is assumed that the plug zone is able to withstand an infinitesimal perturbation without breaking up. The continuity of the velocity components at the yield surface $R_y + h$ gives

$$(\mathbf{U}_b + \mathbf{u}) ([R_y + h]^{-}, z, t) = (\mathbf{U}_b + \mathbf{u}) ([R_y + h]^{+}, z, t), \tag{3.6}$$

where the superscripts \pm indicate that the limit is taken from each side of the yield surface. Since $\mathbf{u} = 0$ uniformly in the plug zone, the linearization of the boundary conditions at the yielded side reads

$$\mathbf{u} = 0 \quad \text{at } r = R_y. \tag{3.7}$$

Additional conditions arise from the von Mises yield criterion and the continuity of stress (i.e. traction) through the fluid domain, which demand that $\dot{\gamma}(\mathbf{U}_b + \mathbf{u}) = 0$ at

the perturbed yield surface (Frigaard, Howison & Sobey 1994; Frigaard & Nouar 2003; Landry *et al.* 2006; Nouar *et al.* 2007). This results in

$$\dot{\gamma}_{rr}(\mathbf{u}) = \dot{\gamma}_{\theta\theta}(\mathbf{u}) = \dot{\gamma}_{zz}(\mathbf{u}) = 0 \quad \text{at } r = R_y, \quad (3.8)$$

$$\dot{\gamma}_{rz}(\mathbf{u}) = \dot{\gamma}_{\theta z}(\mathbf{u}) = 0 \quad \text{at } r = R_y, \quad (3.9)$$

$$\dot{\gamma}_{r\theta}(\mathbf{u}) = \frac{2hB \operatorname{sgn}(\tau_i)}{R_y} \quad \text{at } r = R_y. \quad (3.10)$$

These conditions are not strictly boundary conditions. Instead, (3.8) and (3.9) are compatibility conditions. Indeed, each $\dot{\gamma}_{ij}(\mathbf{u})$ in (3.8) and (3.9) also appears in the Bingham terms (2.32) divided by $\dot{\gamma}(\mathbf{U}_b)$. With these conditions satisfied, all the terms $m_{1,ij}$ in (2.32) remain bounded, and the linear problem is thus well defined. Equation (3.10) is not required for compatibility, since $m_{1,r\theta} = 0$ (see (2.31)). Instead, it defines the perturbation of the yield surface h . Using the normal-mode ansatz of the perturbation, it can be shown straightforwardly that $\dot{\gamma}_{r\theta}(\mathbf{u}) = \partial v / \partial r$ at $r = R_y$. In other words, the yield surface perturbation depends only on the azimuthal component of the velocity disturbance. The strength of Taylor vortices is $\sqrt{u^2 + w^2} = O((r - R_y)^2)$ as $r \rightarrow R_y^-$. Indeed, the compatibility conditions (3.8) and (3.9) reduce to $\partial u / \partial r = \partial w / \partial r = 0$ at $r = R_y$.

Finally, note that there is no kinematic condition since the yield surface is not a material surface or interface.

3.2. Summary of subsequent analysis

In a classical way, the disturbance components of velocity as well as the pressure and the yield surface disturbances are put into normal mode form. An eigenvalue problem is then derived whose numerical solution allows us to obtain the critical values of Reynolds number Re_{1c} , axial wavenumber k_c and azimuthal wavenumber m_c at the onset of the instability as a function of Bingham number and external Reynolds number. In particular, we have determined the ranges of B and Re_2 for which the instability is axisymmetric. A detailed analysis is given in § 2 of the supplementary material.

Finally, note that for the case I basic flow, the finite plug that fills the annulus cannot be perturbed by an infinitesimal perturbation. Therefore, in this case there is no linear stability problem.

4. Weakly nonlinear analysis

From here on, we consider only axisymmetric disturbances. In this case, the continuity equation simplifies and is satisfied via introduction of a function ϕ such that

$$u = -\frac{\partial \phi}{\partial z} \quad \text{and} \quad w = \frac{1}{r} \frac{\partial}{\partial r}(r\phi). \quad (4.1a,b)$$

The pressure is eliminated by cross-differentiating the radial and axial momentum equations. Finally, the perturbation equations are written in terms of $\mathbf{f} = (\phi, v)^T$ as

$$C \frac{\partial \mathbf{f}}{\partial t} = \mathbf{L}\mathbf{f} + \mathbf{N}(\mathbf{f}), \quad (4.2)$$

where again L and N denote linear and nonlinear operators, respectively. They are split into inertial, viscous and yield stress parts as

$$L = Re_1 LI + LV + BLY, \tag{4.3}$$

$$N = Re_1 NI + BNY. \tag{4.4}$$

4.1. Multiple scales method

As the Reynolds number is increased above the onset Re_{1c} , the growth rate of the perturbation is positive for any wavenumber k within a band $\sqrt{\epsilon}$ around the critical wavenumber, where $\epsilon = (Re_1 - Re_{1c})/Re_{1c}$ is the distance from the onset. Taylor expansion of the dispersion curve near its maximum shows that $s \propto \epsilon$ and $(k - k_c) \propto \sqrt{\epsilon}$. For $\epsilon > 0$, the solution of the nonlinear problem can be described by a sum of unstable modes of the form $\exp(st/\tau_0) \exp(ikcz) \exp(i\sqrt{\epsilon}z/\xi_0)$, where τ_0 is the characteristic time for the instability to grow, and ξ_0 is the coherence length, i.e. a characteristic length scale that governs the spatial modulation of the solution. In a similar vein, Manneville & Czarny (2009) interpret ξ_0 as a measure of how easily the unstable mode can accommodate modulations. For small ϵ , we can separate the dynamics into fast eigenmodes and slow modulation of the form $\exp(s\epsilon/\tau_0)$ and $\exp(i\sqrt{\epsilon}z/\xi_0)$. We denote $\delta = \sqrt{\epsilon}$. The multiple scales approach is used to obtain the amplitude equation, which describes the slow temporal and spatial variation of the variables. The slow scales

$$Z = \delta z \quad \text{and} \quad T = \delta^2 t \tag{4.5a,b}$$

are treated as independent of the fast scales z and t . The derivatives with respect to the new variables are

$$\frac{\partial}{\partial t} \rightarrow \frac{\partial}{\partial t} + \delta^2 \frac{\partial}{\partial T}, \quad \frac{\partial}{\partial z} \rightarrow \frac{\partial}{\partial z} + \delta \frac{\partial}{\partial Z}. \tag{4.6a,b}$$

The fast spatial variables vary on the order of a typical wavelength. The slow variables describe the temporal and spatial modulations of these fast variables. Furthermore, as the marginal mode is stationary, we have

$$\frac{\partial}{\partial t} \rightarrow \delta^2 \frac{\partial}{\partial T}. \tag{4.7}$$

In the neighbourhood of the critical conditions, corresponding to the onset of convection, the solution is expanded in powers of δ :

$$f = \delta f_1 + \delta^2 f_2 + \delta^3 f_3 + O(\delta^4), \tag{4.8}$$

$$Re_1 = Re_{1c} + \delta^2 Re_1^{(2)} + O(\delta^4). \tag{4.9}$$

The Reynolds number is increased by increasing the rotation rate of the inner cylinder. Therefore, the Bingham number will be perturbed as

$$B + \delta^2 B^{(2)} = B - \delta^2 \frac{B}{Re_{1c}} Re_1^{(2)} + O(\delta^4), \tag{4.10}$$

where B is the Bingham number that is used in the determination of the critical conditions. Actually, in (4.10), we have written $B = He/Re_1$, where He is the Hedström number. In the

case II, where the fluid is partially yielded, the yield surface at $r = R_y$ is disturbed to

$$r = R_y + \delta h_1 + \delta^2 \tilde{h}_2 + \delta^3 h_3 + O(\delta^4). \quad (4.11)$$

It is worth noting that the second-order perturbation term above \tilde{h}_2 includes the change in the Bingham number due to the change in Re from Re_c to $Re_c + \delta^2 Re^{(2)}$, as the angular rotation of the inner cylinder is increased. This second-order change in the Reynolds number leads effectively to a change in the dimensionless yield stress, which in turn shifts the position of the yield surface:

$$\tilde{h}_2 = h_2 - \frac{B}{Re_{1c}} Re_1^{(2)} \left(\frac{dR_y}{dB} \right)_c. \quad (4.12)$$

Since there are temporal and spatial derivatives $\partial/\partial t$ and $\partial/\partial z$ in operators \mathbf{C} , \mathbf{L} and \mathbf{N} as introduced in (4.2)–(4.4), these operators also need to be expanded as series in δ :

$$\mathbf{C} = \mathbf{C}_0 + \delta \mathbf{C}_1 + O(\delta^2), \quad (4.13)$$

$$\mathbf{L}\mathbf{I} = \mathbf{L}\mathbf{I}_0 + \delta \mathbf{L}\mathbf{I}_1 + \delta^2 \mathbf{L}\mathbf{I}_2 + O(\delta^3), \quad (4.14)$$

$$\mathbf{N}\mathbf{I} = \delta^2 \mathbf{N}\mathbf{I}_2 + \delta^3 \mathbf{N}\mathbf{I}_3 + O(\delta^4), \quad (4.15)$$

$$\mathbf{N}\mathbf{Y} = \delta^2 \mathbf{N}\mathbf{Y}_2 + \delta^3 \mathbf{N}\mathbf{Y}_3 + O(\delta^4). \quad (4.16)$$

Formally, Taylor expansions of $\mathbf{L}\mathbf{V}$ and $\mathbf{L}\mathbf{Y}$ are similar to that of the inertial linear operator $\mathbf{L}\mathbf{I}$. The explicit expressions of \mathbf{C} , $\mathbf{L}\mathbf{I}$, $\mathbf{L}\mathbf{V}$, $\mathbf{L}\mathbf{Y}$, $\mathbf{N}\mathbf{I}$ and their subscales are given in § 3 of the supplementary material.

4.2. Derivation of the Ginzburg–Landau equation

We substitute (4.6a,b), (4.7) and (4.13)–(4.16) into (4.2) and collect the terms at the same order of δ . In the following, the first three orders in δ are developed, and the Ginzburg–Landau equation is derived by applying the solvability condition to the equation written at order δ^3 .

For axisymmetric perturbations, the linear stability analysis suggests an exchange of stability as we traverse Re_{1c} . Thus in the classical way, we look for periodic solutions of the form

$$\begin{aligned} \mathbf{f} = & \delta \left[A \mathbf{f}_1^{(1)} E^1 + \text{c.c.} \right] + \delta^2 \left[|A|^2 \mathbf{f}_2^{(0)} E^0 + A^2 \mathbf{f}_2^{(2)} E^2 + \text{c.c.} \right] \\ & + \delta^3 \left[|A|^2 A \mathbf{f}_3^{(1)} E^1 + A^3 \mathbf{f}_3^{(3)} E^3 + \text{c.c.} \right] + \dots, \end{aligned} \quad (4.17)$$

where the subscript refers to the order in δ , and the superscript to the corresponding Fourier mode, with

$$\mathbf{f}_j^{(i)} = [F_{ij}, V_{ij}] \quad \text{and} \quad E^n = e^{ink_c z}. \quad (4.18a,b)$$

In (4.17), the amplitude $A = A(Z, T)$ of the perturbation depends on slow variables. Furthermore, we have assumed that the amplitudes of the higher-frequency spatial

modes, which require interactions between lower-frequency modes, will scale accordingly. Similarly, the perturbation h of the yield surface is assumed to be of the form

$$h = \delta \left[AH_{11}E^1 + \text{c.c.} \right] + \delta^2 \left[|A|^2 \bar{H}_{02}E^0 + A^2 H_{22}E^2 + \text{c.c.} \right] + \delta^3 \left[|A|^2 AH_{13}E^1 + A^3 H_{33}E^3 + \text{c.c.} \right] + \dots \quad (4.19)$$

As far as the boundary conditions are concerned, in case III of the base solution (fluid fully yielded), the no-slip condition is used at the inner and outer walls. In case II of the base solution (fluid partially yielded), the conditions of continuity of velocity and stress at the disturbed yield surface are considered. They are described in detail in § 4 of the supplementary material.

Finally, gathering powers of E at each order in δ , we derive the following hierarchical structure.

4.2.1. Solution at order δ

At the first order, we recover the linear problem

$$L_0 f_1^{(1)} = 0. \quad (4.20)$$

In case III of the base solutions (fully yielded) the no-slip conditions at the walls give

$$F_{11} = DF_{11} = V_{11} = 0 \quad \text{at } r = R_1, R_2. \quad (4.21)$$

In case II of the base solutions (partially yielded), the boundary conditions at the inner wall are identical to those in case III. At the yield surface, combining the continuity of velocity and yield conditions leads to

$$F_{11} = DF_{11} = D^2 F_{11} = 0 \quad \text{at } r = R_y, \quad (4.22)$$

$$V_{11} = 0 \quad \text{at } r = R_y, \quad (4.23)$$

$$DV_{11} = -H_{11} D^2 V_b \quad \text{at } r = R_y. \quad (4.24)$$

Any multiple of an eigenfunction is also a solution of the linear problem (4.20), and in order to define a reference solution, F_{11} and V_{11} can be normalized such that

$$\max(V_{11}) = 1, \quad (4.25)$$

which fixes the amplitude of the perturbation. Computations indicate that the eigenfunction F_{11} is pure imaginary while V_{11} is real. As an example, figure 5 shows the structure of the critical eigenfunctions obtained for a wide gap, $\eta = 0.4$. The main features are as follows. For small values of $0 \leq B \leq 0.88$, we have the case III basic solution: fully yielded fluid filling the annular gap. In this range of B , the maximum of V_{11} and F_{11} is shifted towards the inner wall, with a significant decrease of the maximum of F_{11} . As B increases, the critical eigenfunctions are non-zero only in a progressively smaller yielded layer of width $(R_y - R_1)$.

As for the basic flow, it can be shown that every case II stability problem maps to a case II–III stability problem. This procedure is quite common in linear stability problems of viscoplastic fluid (Landry *et al.* 2006; Nouar *et al.* 2007). Indeed, if we rescale the radial distance as for the basic flow and use the definitions $\tilde{k} = k(R_0 - R_1)$, $\tilde{s} = s(R_0 - R_1)^2$, $\tilde{Re}_1 = Re_1 (R_0 - R_1)$ and $\tilde{Re}_2 = Re_2 R_0(1 - \eta)(R_0 - R_1)$, then we recover an identical

Taylor vortices in yield stress fluids

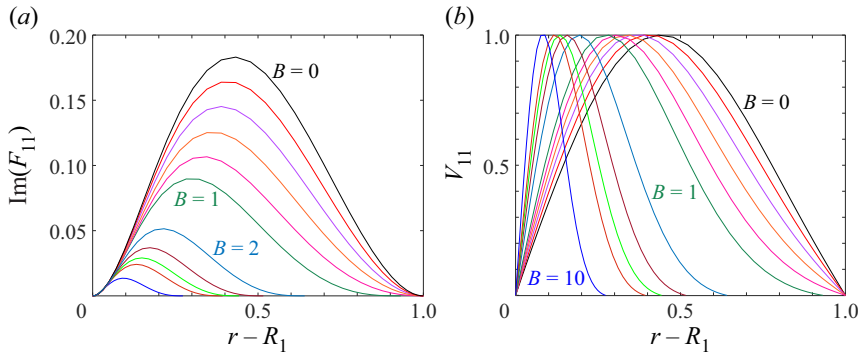


Figure 5. Eigenfunctions (a) $\text{Im}(F_{11})$ and (b) V_{11} associated with the critical mode at $\eta = 0.4$ for different values of B : 0, 0.2, 0.4, 0.6, 0.8, 1, 2, 3, 4, 5, 10.

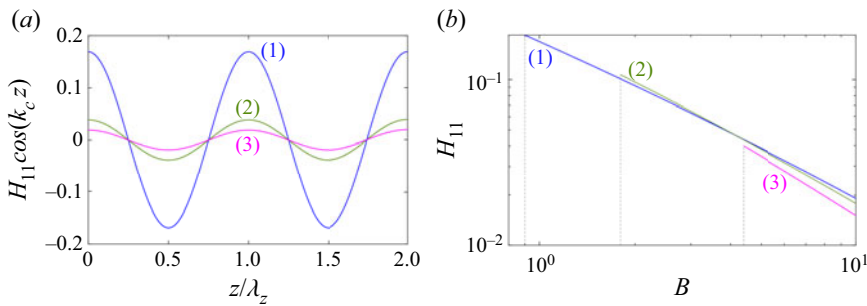


Figure 6. (a) Perturbation of the yield surface associated with the critical mode at $\eta = 0.4$ for three different values of the Bingham number: (1) $B = 1$, (2) $B = 5$ and (3) $B = 10$. (b) Variation of H_{11} as a function of B for three different values of the radius ratio: (1) $\eta = 0.4$, (2) $\eta = 0.6$ and (3) $\eta = 0.8$. Vertical dashed lines indicate the value of B from which a static layer appears on the outer cylinder.

eigenvalue problem. The mapping was made possible because the boundary conditions are homogeneous (Landry *et al.* 2006).

In figure 6(a) we have represented the yield surface perturbations by the linear mode $H_{11}E^1$, along the reduced axial position z/λ_z , where $\lambda_z = 2\pi/k_c$ is the axial wavelength. The case II of the base flow is considered with different values of the Bingham number. The minimum of $\text{Re}(H_{11}E^1)$ corresponds to the jet impingement near the yield surface, and the maximum to the radial flow from the outer to the inner cylinder. It can also be noticed in figure 6(b) that H_{11} decreases significantly with increasing Bingham number.

4.2.2. Linear adjoint mode

The adjoint mode is required to obtain the Ginzburg–Landau equation. Its definition is given as

$$\langle \mathbf{f}_{ad}, \mathbf{L}\mathbf{f}_1 \rangle = \langle \mathbf{L}_{ad}\mathbf{f}_{ad}, \mathbf{f}_1 \rangle, \quad (4.26)$$

where $\mathbf{f}_{ad} = [F_{ad}, V_{ad}]^T$ is the adjoint eigenfunction, \mathbf{L} is the linear stability operator, and $\mathbf{L}_{ad} = \text{Re}_1 \mathbf{L}\mathbf{I}_{ad} + \mathbf{L}V_{ad} + B\mathbf{L}Y_{ad}$ is the corresponding adjoint operator. In this definition, the inner product is given as

$$\langle \mathbf{f}, \mathbf{g} \rangle = \int_{R_1}^{R_0} \mathbf{f}^* \cdot \mathbf{g} r dr, \quad (4.27)$$

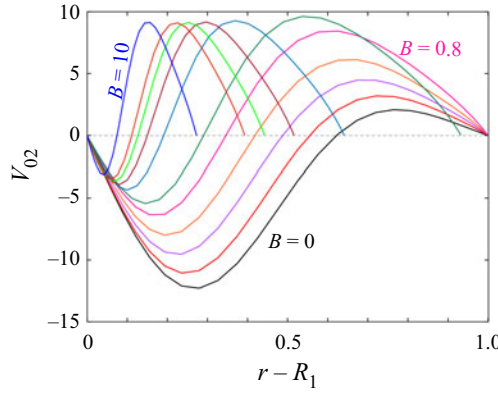


Figure 7. Wide gap geometry with $\eta = 0.4$. Modification of the base flow at the second order in δ for $B = 0, 0.2, 0.4, 0.6, 0.8, 1, 2, 3, 4, 5, 10$.

where f^* is the complex conjugate of f . We find that $C_{(\ell)}$, $LV_{(\ell)}$ and $LY_{(\ell)}$ ($\ell = 0, 1, 2$) are real and self-adjoint, whereas $LI_{(\ell)}$ is not self-adjoint. We have

$$LI_{ad} = \begin{pmatrix} 0 & -ik_c D_* V_b \\ 2ik_c V_b / r & 0 \end{pmatrix}. \tag{4.28}$$

The linear adjoint problem

$$L_{ad}(f_{ad}) = 0 \tag{4.29}$$

is subject to appropriate boundary conditions, matching those of the linear problem, i.e. (4.21), (4.22) and (4.23). As the adjoint is linear and can be scaled arbitrarily, we normalize the adjoint eigenfunctions so that the maximum of the adjoint azimuthal velocity is $\max(V_{ad}) = 1$.

4.2.3. Solution at order δ^2 : quadratic modes

At order δ^2 , the solution has two components. The first component, proportional to $|A|^2 E^0$, arises from the nonlinear interaction of the fundamental mode with its complex conjugate, and the second one, proportional to $A^2 E^2$, arises from the nonlinear interaction of the fundamental mode with itself.

First, consider mode 0, factor $|A|^2 E^0$.

This harmonic is a correction at the second order of the base flow. It is obtained by solving the system of equations

$$L_0 f_2^{(0)} = -Re_{1c} \left[NI \left(f_1^{(1)} |f_1^{(-1)} \right) \right]_{|A|^2 E^0} - B \left[NY \left(f_1^{(1)} |f_1^{(-1)} \right) \right]_{|A|^2 E^0}, \tag{4.30}$$

where $f_1^{(-1)} = f_1^{(1)*}$ is the complex conjugate of $f_1^{(1)}$. As previously, the boundary conditions are of two types.

In case II of the base solutions, the no-slip condition at the walls gives

$$F_{02} = DF_{02} = V_{02} = 0 \quad \text{at } r = R_1, R_2. \tag{4.31}$$

Taylor vortices in yield stress fluids

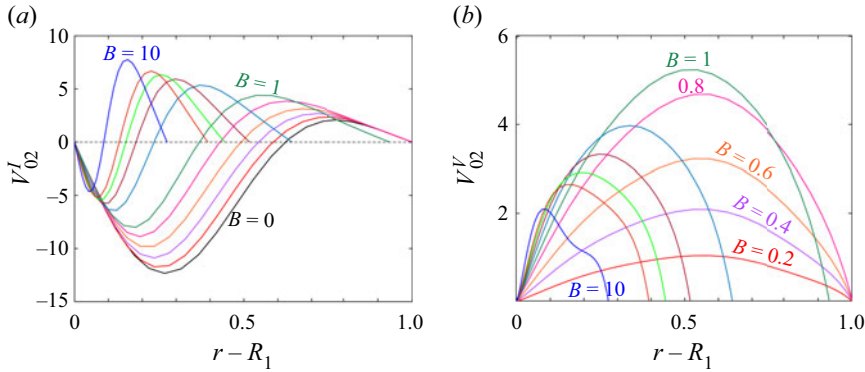


Figure 8. Wide gap geometry with $\eta = 0.4$. Modification of the base flow at the second order in δ . (a) Contribution of the nonlinear inertia terms for $B = 0, 0.2, 0.4, 0.6, 0.8, 1, 2, 3, 4, 5, 10$. (b) Contribution of the nonlinear viscous terms for the same values of B .

In case III of the base solutions, the boundary conditions and yield conditions at the yield surface lead to

$$F_{02} = DF_{02} = 0 \quad \text{at } r = R_y, \tag{4.32}$$

$$D^2F_{02} = - \left[H_{11}D^3F_{11}^* + H_{11}^*D^3F_{11} \right] \quad \text{at } r = R_y, \tag{4.33}$$

$$V_{02} = H_{11}H_{11}^*D^2V_b \quad \text{at } r = R_y. \tag{4.34}$$

As for the linear eigenfunction, the nonlinear corrections are computed numerically. The results show, as expected, that $F_{02} = 0$, i.e. there is no radial or axial mean flow. The correction at the second order of the azimuthal velocity profile of the base state is illustrated by the profiles of V_{02} represented in figure 7 for different values of B . Near the inner cylinder, $V_{02} < 0$, i.e. the azimuthal velocity is reduced, and near the outer cylinder or near the yield surface, $V_{02} > 0$, i.e. the azimuthal velocity is increased. Actually, the profiles of V_{02} can be related to the outward and inward radial flows. The radial outward flow carries fluid particles with high azimuthal momentum from the inner cylinder, increasing the azimuthal velocity near the outer cylinder. The radial inward flow carries fluid particles with low azimuthal momentum from the outer cylinder, decreasing the azimuthal velocity near the inner cylinder. For a Newtonian fluid, the deficit of the azimuthal velocity is higher than the surplus. With increasing Bingham number, the opposite result is observed. Furthermore, the fluid is yielded in a smaller domain of width $(R_y - R_1)$. Cancelling artificially the nonlinear yield stress terms in (4.30) allows us to highlight the contribution of the nonlinear inertial terms (figure 8a) and *vice versa*, to highlight the contribution of the nonlinear yield stress terms (figure 8b) on the modification of the basic flow. The interaction of the fundamental mode with its complex conjugate through nonlinear yield stress terms accelerates the fluid in the whole yielded fluid domain. A positive correction of the basic azimuthal flow leads to a destabilizing effect and therefore may be considered as a precursor to the emergence of a subcritical bifurcation.

The perturbation of the yield surface by the mode $\tilde{H}_{02}E^0$ is obtained from the yield condition and is given by

$$\tilde{H}_{02}D^2V_b = -DV_{02} - \left[H_{11}D^2V_{11}^* + H_{11}^*D^2V_{11} \right] - H_{11}H_{11}^*D^3V_b \quad \text{at } r = R_y, \tag{4.35}$$

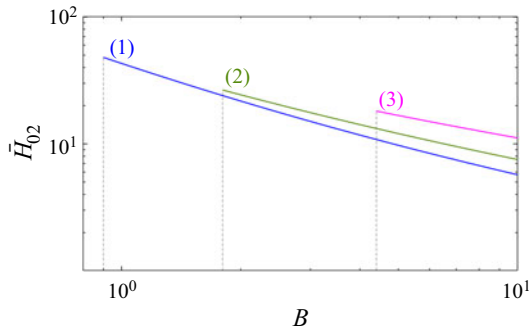


Figure 9. Modification at the second order in δ of the width of the static layer as a function of the Bingham number: (1) $\eta = 0.4$, (2) $\eta = 0.6$ and (3) $\eta = 0.8$. Vertical dashed lines indicate the value of B from which a static layer appears on the outer cylinder.

with $\tilde{H}_{02} = H_{02} + \tilde{H}_0$. The first term arises from the interaction of the fundamental mode with its complex conjugate, and the second term arises from the variation of the Bingham number as the Reynolds number is increased. The variation of \tilde{H}_{02} with the Bingham number is shown in figure 9. Positive values of \tilde{H}_{02} mean that the width of the plug zone is reduced. The reduction is weaker with increasing B . Nevertheless, one can highlight the high values of \tilde{H}_{02} compared with H_{11} . This result shows that in the presence of a static layer, the nonlinear terms become significant quickly.

Now consider the mode 2 factor of A^2E^2 .

The first harmonic mode is a solution of the system of equations

$$L_0 f_2^{(2)} = -Re_{1c} \left[NI \left(f_1^{(1)} | f_1^{(1)} \right) \right]_{A^2E^2} - B \left[NY \left(f_1^{(1)} | f_1^{(1)} \right) \right]_{A^2E^2}, \quad (4.36)$$

with the appropriate boundary conditions.

In case III of the base solutions, the no-slip condition at the walls gives

$$F_{22} = DF_{22} = V_{22} = 0 \quad \text{at } r = R_1, R_2. \quad (4.37)$$

In case II of the base solutions, the boundary conditions and yield conditions at the yield surface lead to

$$F_{22} = DF_{22} = 0 \quad \text{at } r = R_y, \quad (4.38)$$

$$D^2F_{22} = -H_{11}D^3F_{11} \quad \text{at } r = R_y, \quad (4.39)$$

$$V_{22} = \frac{1}{2}H_{11}^2D^2V_b \quad \text{at } r = R_y. \quad (4.40)$$

The influence of Bingham number B on the profiles $\text{Im}(F_{22}(r))$ and $V_{22}(r)$ is shown in figure 10. The maximum of these profiles increases over a short range of B , where the fluid is fully yielded, and then decreases with increasing B , probably as a consequence of the reduction of energy exchange between the fundamental and its harmonic via the nonlinear yield stress terms.

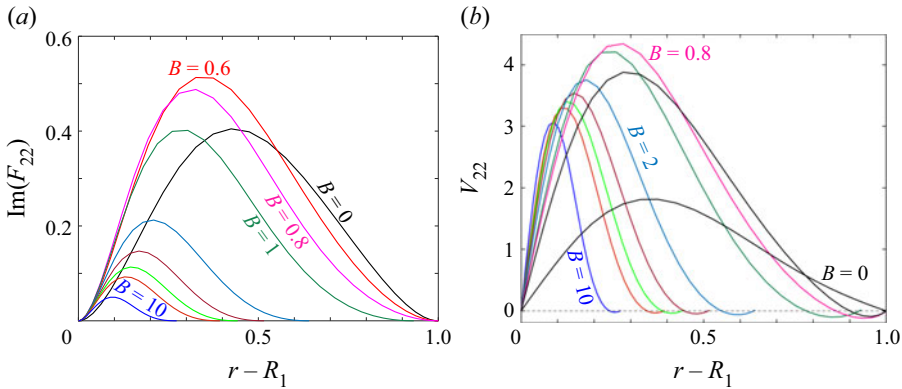


Figure 10. Correction of the linear mode at the second order in δ at critical conditions at $\eta = 0.4$ and for different values of B : 0, 0.2, 0.6, 0.8, 1, 2, 3, 4, 5, 10; (a) $\text{Im}(F_{22}(r))$, and (b) $V_{22}(r)$.

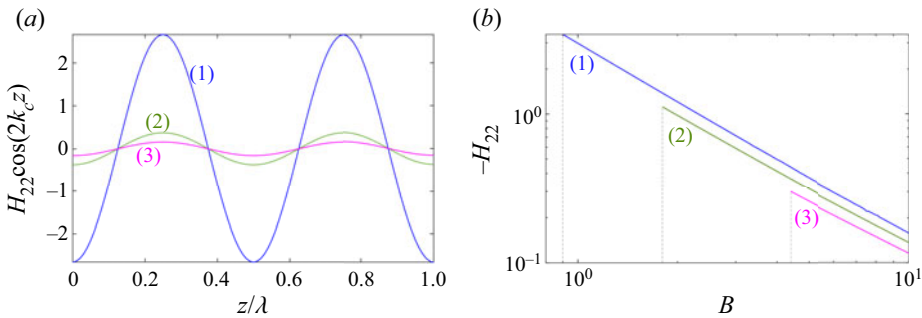


Figure 11. (a) Yield surface perturbation of mode 2 for $\eta = 0.4$ and three different values of B : (1) $B = 1$, (2) $B = 5$ and (3) $B = 10$. (b) Amplitude H_{22} of the second harmonic of the yield surface perturbation as a function of the Bingham number: (1) $\eta = 0.4$, (2) $\eta = 0.6$ and (3) $\eta = 0.8$.

The perturbation of the yield surface by the mode $H_{22}A^2E^2$ is obtained from yield conditions and is given by

$$H_{22}D^2V_b = -DV_{22} - H_{11}D^2V_{11} - \frac{H_{11}^2}{2}D^3V_b \quad \text{at } r = R_y. \quad (4.41)$$

It is represented in figure 11 as a function of B . One notices that: (i) H_{22} decreases with increasing width of the static layer; and (ii) H_{22} is one order of magnitude larger than H_{11} .

Remark. As for the linear problem, there is a similarity mapping that maps V_{02}, F_{22} and V_{22} , obtained in the case where the fluid in the annular space is partially yielded, onto solutions $\tilde{V}_{02}, \tilde{F}_{22} = F_{22}/(R_0 - R_1)$ and \tilde{V}_{22} , obtained for an outer cylinder of radius equal to the yield surface radius.

4.2.4. Solution at order δ^3 : the Ginzburg–Landau equation

At order δ^3 , the solution has two components. The first, proportional to $|A|^2AE^1$, represents the feedback at order δ^3 on the fundamental mode through the nonlinear interactions of the fundamental with the second harmonic, and with the modification of the basic state. The second component is the second harmonic.

The first component, $\mathbf{f}_1^{(3)} = [F_{13}, V_{13}]^T$, satisfies the non-homogeneous equation

$$\begin{aligned} |A|^2 AL_0 \mathbf{f}_3^{(1)} &= C_0 \frac{\partial A}{\partial T} \mathbf{f}_1^{(1)} - Re^{(2)} A \left(LI_0 - \frac{B}{Re_c} LY_0 \right) \mathbf{f}_1^{(1)} - A L_2 \mathbf{f}_1^{(1)} \\ &\quad - Re_{1c} |A|^2 A \left[NI \left(\mathbf{f}_1^{(1)} | \mathbf{f}_2^{(0)} \right) + NI \left(\mathbf{f}_1^{(-1)} | \mathbf{f}_2^{(2)} \right) \right] \\ &\quad - B |A|^2 A \left[NY \left(\mathbf{f}_1^{(1)} | \mathbf{f}_2^{(0)} \right) + NY \left(\mathbf{f}_1^{(-1)} | \mathbf{f}_2^{(2)} \right) \right] \\ &\quad - B |A|^2 A NY \left(\mathbf{f}_1^{(1)}, \mathbf{f}_1^{(1)} | \mathbf{f}_1^{(-1)} \right). \end{aligned} \tag{4.42}$$

Concerning the boundary conditions, for case III of the base solutions, we have

$$F_{13} = DF_{13} = 0 \quad \text{at } r = R_1, R_2, \tag{4.43}$$

$$V_{13} = 0 \quad \text{at } r = R_1, R_2. \tag{4.44}$$

For case II of the base solutions, the boundary conditions combined with the yield conditions at the yield surface are

$$F_{13} = 0, \tag{4.45}$$

$$DF_{13} = H_{11} H_{11}^* D^3 F_{11} + \frac{H_{11}^2}{2} D^3 F_{11}^*, \tag{4.46}$$

$$\begin{aligned} D^2 F_{13} &= -H_{11} H_{11}^* D^4 F_{11} - H_{11}^* D^3 F_{22} - \bar{H}_{02} D^3 F_{11} - H_{22} D^3 F_{11}^* \\ &\quad - \frac{H_{11}^2}{2} D^4 F_{11}^* - \frac{H_{11}}{R_0} \left[H_{11} D^3 F_{11}^* + H_{11}^* D^3 F_{11} \right], \end{aligned} \tag{4.47}$$

$$\begin{aligned} V_{13} &= H_{11} H_{11}^* D^2 V_{11} + \frac{H_{11}^2}{2} D^2 V_{11}^* + H_{11}^2 H_{11}^* D^3 V_b \\ &\quad + (H_{11}^* H_{22} + H_{11} \bar{H}_{02}) D^2 V_b. \end{aligned} \tag{4.48}$$

The condition on DV_{13} defines H_{13} , but is lengthy and omitted for brevity.

The amplitude equation is found in the usual way, as a solvability condition on the third-order problem. In the case where the annular space is fully yielded, the boundary conditions for $\mathbf{f}_1^{(3)}$ are homogeneous. The solvability condition leads to

$$\begin{aligned} 0 &= \left\langle \mathbf{f}_{ad}, C_0 \mathbf{f}_1^{(1)} \right\rangle \frac{\partial A}{\partial T} \\ &\quad - Re^{(2)} \left\langle \mathbf{f}_{ad}, \left(LI_0 - \frac{B}{Re_{1c}} LY_0 \right) \mathbf{f}_1^{(1)} \right\rangle A - \left\langle \mathbf{f}_{ad}, L_2 \mathbf{f}_1^{(1)} \right\rangle A \\ &\quad - Re_{1c} \left\langle \mathbf{f}_{ad}, NI \left(\mathbf{f}_2^{(0)} | \mathbf{f}_1^{(1)} \right) \right\rangle |A|^2 A - Re_{1c} \left\langle \mathbf{f}_{ad}, NI \left(\mathbf{f}_2^{(2)} | \mathbf{f}_1^{(-1)} \right) \right\rangle |A|^2 A \\ &\quad - B \left\langle \mathbf{f}_{ad}, NY \left(\mathbf{f}_2^{(0)} | \mathbf{f}_1^{(1)} \right) \right\rangle |A|^2 A - B \left\langle \mathbf{f}_{ad}, NY \left(\mathbf{f}_2^{(2)} | \mathbf{f}_1^{(-1)} \right) \right\rangle |A|^2 A \\ &\quad - B \left\langle \mathbf{f}_{ad}, NY \left(\mathbf{f}_1^{(1)}, \mathbf{f}_1^{(1)} | \mathbf{f}_1^{(-1)} \right) \right\rangle |A|^2 A. \end{aligned} \tag{4.49}$$

Using the departure from the linear threshold

$$\epsilon = \frac{Re_1 - Re_{1c}}{Re_{1c}} = \delta^2 \frac{Re^{(2)}}{Re_{1c}}, \tag{4.50}$$

and after returning to the fast variables

$$\delta A(Z, T) = A'(z, t), \quad \frac{\partial}{\partial Z} = \frac{1}{\delta} \frac{\partial}{\partial z} \quad \text{and} \quad \frac{\partial}{\partial T} = \frac{1}{\delta^2} \frac{\partial}{\partial t}, \quad (4.51)$$

the following Ginzburg–Landau equation is derived:

$$\frac{\partial A}{\partial T} = \frac{\epsilon}{\tau_0} A + \frac{\xi_0^2}{\tau_0} \frac{\partial^2 A}{\partial z^2} + g_1 |A|^2 A. \quad (4.52)$$

In (4.52), we have dropped the prime in A' and we expect no confusion to the reader. In this equation, τ_0 is the characteristic time for the instability to grow,

$$\tau_0^{-1} = Re_{1c} \frac{\left\langle \mathbf{f}_{ad}, \left(LI_0 - \frac{B}{Re_{1c}} LY_0 \right) \mathbf{f}_1^{(1)} \right\rangle}{\left\langle \mathbf{f}_{ad}, C_0 \mathbf{f}_1^{(1)} \right\rangle}, \quad (4.53)$$

ξ_0 is the coherence length,

$$\xi_0^2 = \frac{1}{Re_{1c}} \frac{\left\langle \mathbf{f}_{ad}, L_2 \mathbf{f}_1^{(1)} \right\rangle}{\left\langle \mathbf{f}_{ad}, \left(LI_0 - \frac{B}{Re_{1c}} LY_0 \right) \mathbf{f}_1^{(1)} \right\rangle}, \quad (4.54)$$

and g_1 is the first Landau coefficient,

$$\begin{aligned} g_1 = & Re_{1c} \frac{\left\langle \mathbf{f}_{ad}, NI \left(\mathbf{f}_2^{(0)} | \mathbf{f}_1^{(1)} \right) \right\rangle}{\left\langle \mathbf{f}_{ad}, C_0 \mathbf{f}_1^{(1)} \right\rangle} + Re_{1c} \frac{\left\langle \mathbf{f}_{ad}, NI \left(\mathbf{f}_2^{(2)} | \mathbf{f}_1^{(-1)} \right) \right\rangle}{\left\langle \mathbf{f}_{ad}, C_0 \mathbf{f}_1^{(1)} \right\rangle} \\ & + B \frac{\left\langle \mathbf{f}_{ad}, NY \left(\mathbf{f}_2^{(0)} | \mathbf{f}_1^{(1)} \right) \right\rangle}{\left\langle \mathbf{f}_{ad}, C_0 \mathbf{f}_1^{(1)} \right\rangle} + B \frac{\left\langle \mathbf{f}_{ad}, NY \left(\mathbf{f}_2^{(2)} | \mathbf{f}_1^{(-1)} \right) \right\rangle}{\left\langle \mathbf{f}_{ad}, C_0 \mathbf{f}_1^{(1)} \right\rangle} \\ & + B \frac{\left\langle \mathbf{f}_{ad}, NY \left(\mathbf{f}_1^{(1)}, \mathbf{f}_1^{(1)} | \mathbf{f}_1^{(-1)} \right) \right\rangle}{\left\langle \mathbf{f}_{ad}, C_0 \mathbf{f}_1^{(1)} \right\rangle}. \end{aligned} \quad (4.55)$$

The integrals are evaluated numerically by means of the Clenshaw and Curtis method (Trefethen 2000). At critical conditions, and assuming that the amplitude does not vary with the axial position, $\mathbf{f}_1^{(3)} = \mathbf{f}_{1H}^{(3)}$ satisfies an equation of the form

$$L_0 \mathbf{f}_{1H}^{(3)} = g_{1H} C_0 \mathbf{f}_1^{(1)} - Re_{1c} NI - B NY. \quad (4.56)$$

In the case where there is a static layer on the outer wall, the boundary conditions at the yield surface (defined in (4.46)–(4.48)) are inhomogeneous. In order to derive the solvability condition, we decompose, as in Sen & Venkateswarlu (1983) and Bouteraa *et al.* (2015), $\mathbf{f}_1^{(3)}$ into homogeneous ($\mathbf{f}_{1H}^{(3)}$) and inhomogeneous ($\mathbf{f}_{1NH}^{(3)}$) parts:

$$\mathbf{f}_1^{(3)} = \mathbf{f}_{1H}^{(3)} + \mathbf{f}_{1NH}^{(3)}, \quad (4.57)$$

where $\mathbf{f}_{1NH}^{(3)}$ is a correction term that accounts for the non-homogeneity of the boundary conditions. Furthermore, at critical conditions, $\mathbf{f}_1^{(3)}$ satisfies an equation that can be

written as

$$L_0 f_1^{(3)} = g_1 C_0 f_1^{(1)} - Re_{1C} NI - BNY. \tag{4.58}$$

Substituting (4.57) into (4.58), we obtain

$$L_0 f_{1H}^{(3)} = g_1 C_0 f_1^{(1)} - Re_{1C} NI - BNY - L_0 f_{1H}^{(3)}. \tag{4.59}$$

By applying the solvability condition to (4.59), we get

$$g_1 = g_{1H} + \frac{\langle f_{ad}, L_0 f_{1NH}^{(3)} \rangle}{\langle f_{ad}, C_0 f_1^{(1)} \rangle}. \tag{4.60}$$

The technique of solution adopted is to iterate a few times between (4.57) and (4.60). At the start, $f_{1NH}^{(3)}$ is assumed to be identically zero in (4.60). A first approximation of g_1 is then obtained: $g_1^{(1)} = g_{1H}$. This is put into (4.58), which is solved at the critical conditions, with non-homogeneous boundary conditions, to obtain a first approximation of $f_1^{(3)}$. Using (4.57), a first approximation of $f_{1NH}^{(3)}$ is deduced. Then $f_{1NH}^{(3)}$ is put into (4.60). This process is repeated until it converges to a desired level of accuracy. Note that (4.58) is solved with an additional condition

$$f_1^{(3)} = 0 \quad \text{at } r = r_{max}, \tag{4.61}$$

where r_{max} is the radial position at which $V_{11}(r_{max}) = 1$. This normalization was suggested by Herbert (1980, 1983), Sen & Venkateswarlu (1983) and Generalis & Fujimura (2009). Without this normalization, $f_1^{(3)}$ is defined up to an arbitrary multiple of the solution $f_1^{(1)}$. A validation of the procedure used is provided in § 5 of the supplementary material.

5. Results and discussion

5.1. Characteristic time of instability growth and coherence length

The variation of the characteristic time τ_0 , for the instability to grow, as a function of the Bingham number is shown in figure 12(a). As can be observed, τ_0 decreases with increasing B in particular when there is a static layer attached to the outer cylinder, i.e. for $B > 0.88$ at $\eta = 0.4$, and for $B > 8.5$ at $\eta = 0.883$. This result shows that the onset of Taylor vortex flow is faster with increasing B , and even more in the presence of a plug zone on the outer cylinder. To account for the reduction of the annular space in the presence of a static layer on the outer cylinder, τ_0 and B can be rescaled as $\tilde{B} = B(R_y - R_1)$ and $\tilde{\tau}_0 = \tau_0 / (R_y - R_1)^2$. In the representation of $\tilde{\tau}_0$ as a function of \tilde{B} , the slope of the curve is reduced substantially.

Similarly, the coherence length, which can be related to the curvature of the marginal stability curve, decreases with increasing B as shown in figure 12(b). This means that the marginal stability curve flattens with increasing B . The strong decrease of ξ_0 with increasing B , for $B > 0.88$ at $\eta = 0.4$, accounts for the reduction of the width of the annular space where the fluid is yielded. This can be taken into account by using the rescaled parameter \tilde{B} and $\tilde{\xi}_0 = \xi_0 / (R_y - R_1)^2$.

Taylor vortices in yield stress fluids

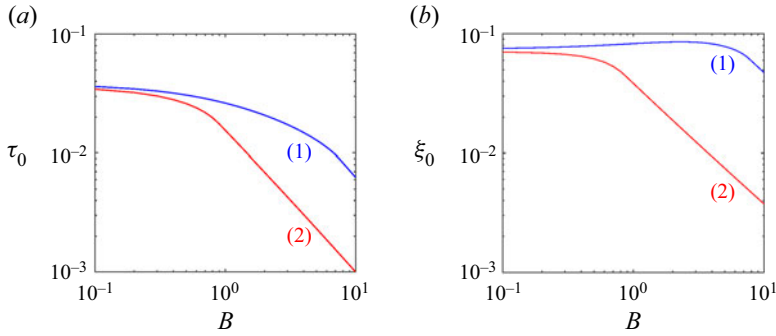


Figure 12. Variations of (a) the characteristic time of instability and (b) the coherence length as functions of the Bingham number for narrow and wide gaps: (1) $\eta = 0.883$, (2) $\eta = 0.4$.

5.2. Transition from supercritical to subcritical bifurcation

In figures 13(a,b), we have represented the variation of the first Landau constant g_1 as a function of the Bingham number for different values of the radius ratio η , with $Re_2 = 0$. The sign of g_1 determines whether we are dealing with a supercritical or a subcritical bifurcation. The following characteristics are noticed.

- (i) For a given radius ratio and at $B = 0$ (Newtonian fluid), g_1 is negative and the bifurcation is supercritical. With increasing B , g_1 decreases, reaches a minimum, then increases rapidly until a particular value of B where the convexity of $g_1(B)$ changes abruptly. Actually, at this particular value of B , a static layer appears on the outer wall.
- (ii) From $\eta \geq \eta_\ell$, with $\eta_\ell = 0.89$ in the present case (thick curve in figure 13a), g_1 is negative and the bifurcation is supercritical for the whole range of values of B considered.
- (iii) For $\eta < \eta_\ell$, g_1 is positive and the bifurcation is subcritical for a range of Bingham numbers whose extent is all the larger as the annular gap is wide. This is illustrated by figure 13(c) where we have represented in the plane (η, B) the boundaries of the subcritical bifurcation domain. Outside this domain, the bifurcation is supercritical.
- (iv) The numerical results show that at the upper boundary of the subcritical bifurcation domain (numbered (3) in figure 13c), the inner to the yield surface radius ratio is $R_1/R_y \approx \eta_\ell$. In other words, when $R_1/R_y > \eta_\ell$, the bifurcation is supercritical.
- (v) At the lower boundary of the subcritical bifurcation domain (numbered (1) in figure 13c), $R_1/R_y = 0.6$. Hence for $\eta < 0.6$, subcritical bifurcation occurs only in presence of a static layer on the outer wall.
- (vi) The minimum value of B at which the primary bifurcation is subcritical is $B = 1.8$, obtained for $\eta = 0.6$.

To shed more light on the mechanism of supercritical/subcritical instability, the first Landau constant is decomposed as

$$g_1 = g_{1I} + g_{1Y} + g_{1NH}, \quad (5.1)$$

where g_{1I} is the contribution of nonlinear inertial terms (terms where Re_{1c} is a factor in (4.55)), g_{1Y} is the contribution of nonlinear yield stress terms (terms where B is a factor in (4.55)), and g_{1NH} is the contribution of non-homogeneous boundary conditions. In figure 14, we have represented the contribution of nonlinear inertial terms and nonlinear

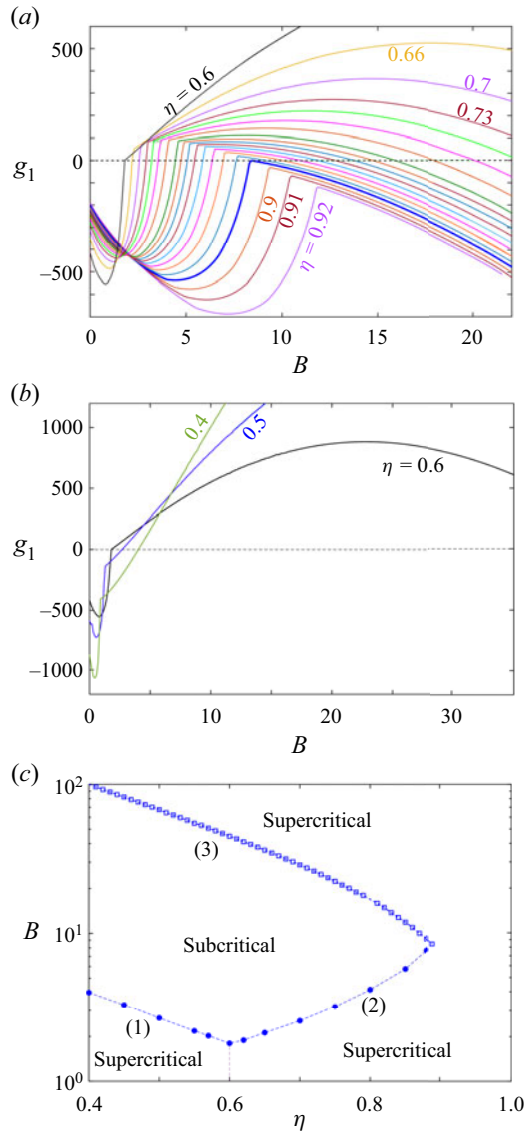


Figure 13. Variation of the first Landau constant as a function of the Bingham number for different values of the radius ratios: (a) from $\eta = 0.92$ until $\eta = 0.81$ by step 0.01, and then $\eta = 0.79, 0.77, 0.75, 0.73, 0.7, 0.66, 0.6$; (b) $\eta = 0.6, 0.5, 0.4$. (c) Boundaries of the subcritical domain in the plane (η, B) : (1) and (2) are the lower boundaries, and (3) is the upper boundary.

yield stress terms to the first Landau constant for different values of η . One can notice the following.

- (i) The value of g_{1I} is negative, and g_{1Y} is positive, i.e. the nonlinear inertial terms promote a supercritical bifurcation leading to saturation of the stationary instability at finite amplitude, whereas the nonlinear yield stress terms promote a subcritical bifurcation. The position of the curve $-g_{1I}$ relative to g_{1Y} accounts for the nature of the primary bifurcation described in figure 13(a). For $\eta \geq \eta_c = 0.89$ (figures 14a,b),

Taylor vortices in yield stress fluids

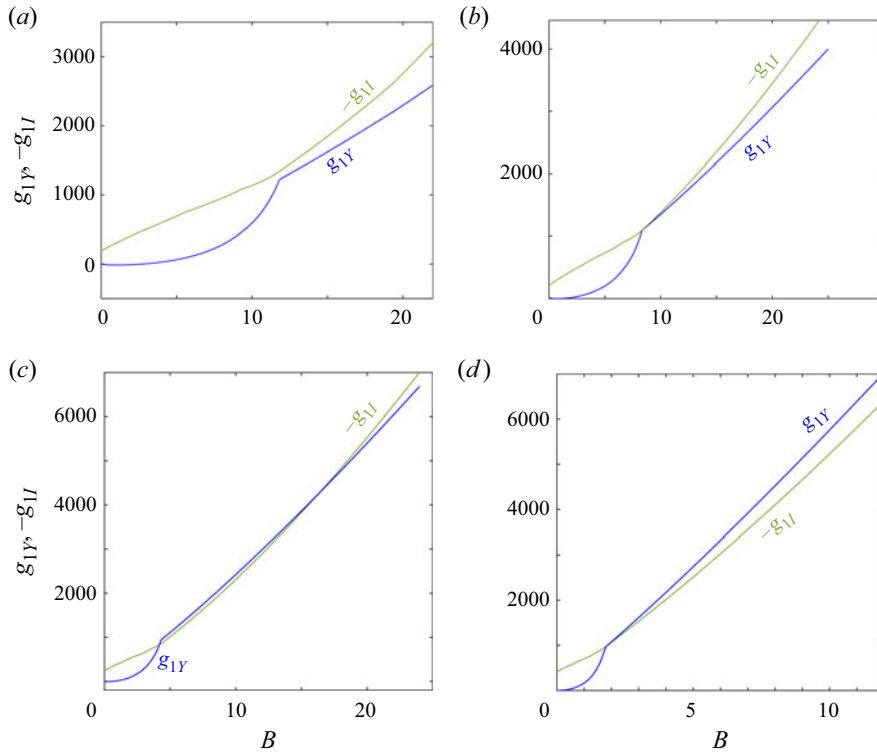


Figure 14. Contributions of nonlinear inertial terms g_{1I} and nonlinear yield stress terms g_{1Y} on the first Landau constant as a function of B for (a) $\eta = 0.92$, (b) $\eta = 0.89$, (c) $\eta = 0.88$, and (d) $\eta = 0.6$.

$(-g_{1I}) > g_{1Y}$ and the bifurcation is supercritical. For $\eta < \eta_\ell$ (figures 14c,d), $(-g_{1I}) > g_{1Y}$ for a range of B close to zero and for large values of B . For intermediate values of B , i.e. between the two crossings of the curves $-g_{1I}(B)$ and $g_{1Y}(B)$ (figure 14c), the bifurcation is subcritical.

- (ii) The values of $(-g_{1I})$ and g_{1Y} increase with B but differently depending on whether the annular space is fully or partially yielded.
- (iii) The abrupt change in the convexity of $g_1(B)$ observed in figures 13(a,b) arises from the change in the curvature of $g_{1Y}(B)$ when a static layer appears on the outer cylinder.
- (iv) As for the non-homogeneous boundary conditions, the obtained values of g_{1NH} show that they promote a subcritical bifurcation. However, their contribution remains very weak, almost 10^{-3} smaller than $(-g_{1I})$, as is shown in figure 7 of the supplementary material. Therefore, g_{1NH} does not play a significant role in the transition from supercritical to subcritical bifurcation.

Obviously, the increase of $-g_{1I}$ with increasing B has to be due to changes with B , in either Re_{1c} or in the factor term of Re_{1c} in (4.55). This last term contains quadratic products of the eigenfunctions and their derivatives that are non-zero in a progressively smaller yielded fluid domain. The numerical results show that more than 99% of the variation of g_{1I} arises from the variation of Re_{1c} as B increases. Furthermore, it is observed that $-g_{1I}$ can be fitted by an affine function of Re_{1c} , with different coefficients, in partially and fully yielded domains. The factor term of Re_{1c} in (4.55) varies mainly with η .

Regarding the variation of g_{1Y} with B , where g_{1Y} can be written formally as $g_{1Y} = B \langle f_{ad}, NY \rangle / \langle f_{ad}, C_0 f^{(1)} \rangle$, two situations must be distinguished, depending on whether the annular space is fully or partially yielded.

The first situation, where the annular space is fully yielded, is as we have a purely viscous shear-thinning fluid. The numerical results show that the increase of g_{1Y} with increasing B can be fitted by a cubic polynomial. The nonlinear yield stress term NY derived from mk_{ij} expressions (2.31)–(2.36) contains products of eigenfunctions and their derivatives divided by $\dot{\gamma}^k(U_b)$ ($k = 1, 2, 3$). It is precisely these terms, i.e. $1/\dot{\gamma}^k(U_b)$, that are responsible for the strong increase in g_{1Y} with increasing B . Indeed, at the outer wall and at critical conditions, $\dot{\gamma}(U_b)|_{R_2}$ decreases linearly with increasing B , and tends to zero as B approaches B_{sl} , the value of B at which a static layer appears at the outer wall, i.e. $\dot{\gamma}(U_b)|_{R_2} \propto (B_{sl} - B)$. Therefore, $1/\dot{\gamma}(U_b)|_{R_2}$ increases sharply, allowing the nonlinear yield stress term to become dominant as $B \rightarrow B_{sl}$.

In the second situation, where the annular space is partially yielded, g_{1Y} increases linearly with B . The quantity $\langle f_{ad}, NY \rangle / \langle f_{ad}, C_0 f^{(1)} \rangle$ remains almost constant as B increases. Here, the characteristics of the flow just after yielding, where $\dot{\gamma}(U_b) \rightarrow 0$, play the dominant role. Recall that the compatibility conditions (equations (4.8)–(4.13) of the supplementary material) ensure that the limit of NY is finite when $\dot{\gamma}(U_b)$ tends to zero.

Remarks.

- (i) A detailed study of the contribution of the different terms that intervene in the g_{1I} and g_{1Y} expressions (4.55) is provided in § 5 of the supplementary material. The data show that the feedback of the mean flow correction plays an important role.
- (ii) For counter-rotating and co-rotating cylinders, variations of the first Landau constant g_1 , the contribution of nonlinear inertial terms g_{1I} and that of nonlinear yield stress terms g_{1Y} as a function of the Bingham number, are qualitatively similar to those obtained for a fixed outer cylinder. They are described in §§ A.1 and A.2.

5.3. Stationary amplitudes

A steady solution of (4.52) is

$$A = A_0 e^{iqz}, \quad \text{with } A_0 = \left| \frac{\epsilon - \xi_0^2 q^2}{\tau_0(-g_1)} \right|^{1/2} \quad \text{and } q = k - k_c. \tag{5.2}$$

Figure 15 shows the bifurcation diagram obtained in the case where $k = k_c$, i.e. $q = 0$, at different Bingham numbers. For a wide gap, $\eta = 0.4$, near the critical conditions, the stable stationary equilibrium amplitude in the supercritical regime is shown in continuous line. At low values of B ($B \leq 0.5$), the nonlinearities dominated by the nonlinear inertial terms are stabilizing. The nonlinear effects associated with the viscosity perturbation, i.e. NY terms, start to become significant from $B = 0.5$ (minimum of $g_1(B)$), leading to a strong increase of the amplitude as B increases. This effect becomes more pronounced from a Bingham number $B = 0.88$ at which a static layer appears on the outer cylinder, with a strong decrease of τ_0 with increasing B . When the bifurcation is subcritical, the threshold amplitude, which limits the basin of attraction of the circular Couette flow, shown in dashed line, decreases with increasing B , i.e. the basic flow becomes more sensitive to finite-amplitude perturbations. However, this variation cannot continue. Indeed, when the width of the yielded zone is sufficiently narrow, $R_1/R_y \geq \eta_\ell$ ($\eta_\ell = 0.89$ when the outer cylinder is fixed), the bifurcation again becomes supercritical. For a narrow

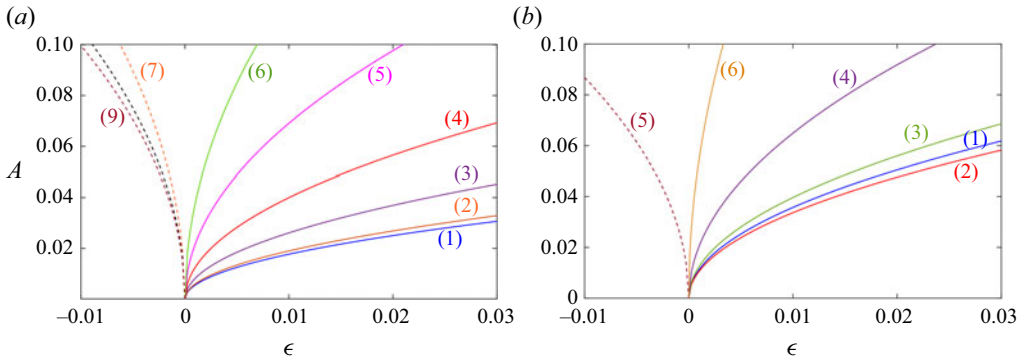


Figure 15. Stationary amplitude as a function of the distance ϵ to criticality. (a) Wide gap, $\eta = 0.4$: (1) $B = 0$, (2) $B = 0.5$, (3) $B = 0.8$, (4) $B = 1$, (5) $B = 2$, (6) $B = 3$, (7) $B = 6$, (8) $B = 8$, (9) $B = 10$. (b) Narrow gap, $\eta = 0.883$: (1) $B = 0$, (2) $B = 1$, (3) $B = 5$, (4) $B = 7$, (5) $B = 8$, (6) $B = 12$.

gap, here $\eta = 0.883$, similar effects are observed in overall (see figure 15b), except that the nonlinear terms NY start to become significant from $B = 4$, with a significant increase in amplitude as B increases. The appearance of a static layer at the outer cylinder occurs in the subcritical domain, and the return to a supercritical bifurcation takes place at $B = 9$.

5.4. Flow structure

One has to note that the numerical values of the Landau constant, and hence the values of the amplitude, depend on the normalization condition used for the eigenfunctions in the linear theory. However, physical quantities such as velocity components, kinetic energy or torque are independent of the normalization. In figure 16, we have represented the profiles of the radial velocity component

$$u = -\left(ik_c A F_{11} E^1 + 2ik_c A^2 F_{22}^* E^2 + \text{c.c.}\right) + O(A^3) \quad (5.3)$$

at $z = 0$, $\epsilon = 0.01$, in a wide gap and a narrow gap, and for different Bingham numbers. These profiles represent the outward radial flow between the inner and outer cylinders, near the onset of the Taylor vortex flow regime. For values of B small enough comparatively to that for which a plug zone appears on the outer cylinder, the increase of $|g_{1I}|$ with B is much more significant than that of g_{1Y} with B (figure 14), and overall, $|g_1|$ increases (figure 13), leading to a decrease in the perturbation amplitude (5.2) and therefore to that of the radial velocity as B increases; see curves (1) and (2) in figure 16(a), and curves (1), (2) and (3) in figure 16(b). However, as B approaches the value associated with the appearance of the plug zone, the increase in g_{1Y} with B (parabolic) becomes significant, and overall, the value of $|g_1|$ begins to decrease, resulting in an increase in amplitude, and thus an increase in the radial velocity; see curves (3) and (4) in figure 16(a), and curves (4) and (5) in figure 16(b).

The evolutions of the axial velocity profiles as functions of B follow the same trends as those described for u . They are therefore not shown.

Outward and inward radial flows carry high azimuthal momentum fluxes from near the inner to the outer cylinder, and low momentum fluxes from near the outer to the inner cylinder, respectively. These result in the formation of positive and negative

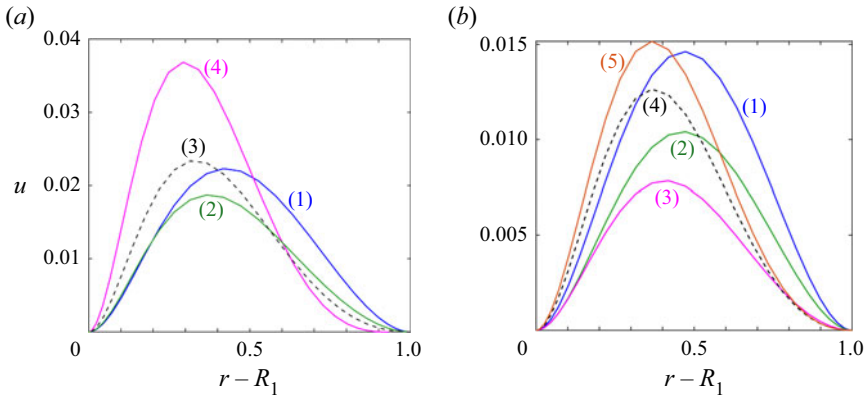


Figure 16. Radial velocity component u across the gap at $z = 0$, $\epsilon = 0.01$, $Re_2 = 0$ and for different Bingham numbers. (a) Wide gap, $\eta = 0.4$: (1) $B = 0$, (2) $B = 0.5$, (3) $B = 0.8$, (4) $B = 1$. (b) Narrow gap, $\eta = 0.883$: (1) $B = 0$, (2) $B = 1$, (3) $B = 5$, (4) $B = 7$, (5) $B = 7.2$.

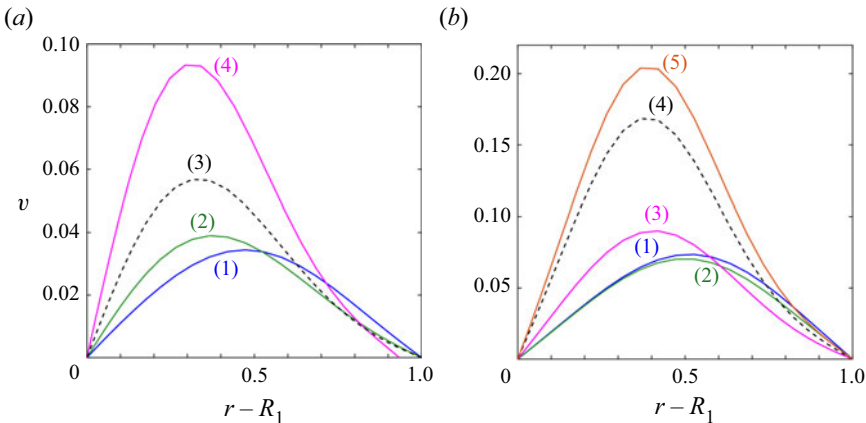


Figure 17. Azimuthal velocity component v across the gap at $z = 0$, $\epsilon = 0.01$, $Re_2 = 0$ and for different Bingham numbers. (a) Wide gap, $\eta = 0.4$: (1) $B = 0$, (2) $B = 0.5$, (3) $B = 1$, (4) $B = 1.4$. (b) Narrow gap, $\eta = 0.883$: (1) $B = 0$, (2) $B = 1$, (3) $B = 5$, (4) $B = 7$, (5) $B = 7.2$.

azimuthal streaks. They are determined by the azimuthal velocity expression

$$v = AV_{11} + A^2V_{22} + |A|^2V_{02} + c.c. + O(A^3). \quad (5.4)$$

Again, at low values of B , the nonlinear inertial terms are dominant and have a stabilizing effect. Once, the nonlinear yield stress terms become significant, the intensity of the azimuthal streaks increases strongly with B , and even more in the presence of a static layer, as shown in figure 17.

The change in the flow structure when departing from the critical conditions modifies the second invariant $\dot{\gamma}$ of the strain rate tensor $\dot{\boldsymbol{\gamma}}$ and thus the effective viscosity.

In figure 18, we show the contours of the stream function $\psi = r\phi$ at $\epsilon = 0.5 \times 10^{-2}$ (figure 18a), which will serve as a guide for the description of the results, and the contours of $\dot{\gamma}$ at $\epsilon = 0$ (figure 18b) and at $\epsilon = 0.5 \times 10^{-2}$ (figure 18c). The case of a wide gap, $\eta = 0.5$, is considered with stationary outer cylinder and $B = 1$ (fluid partially yielded).

Taylor vortices in yield stress fluids

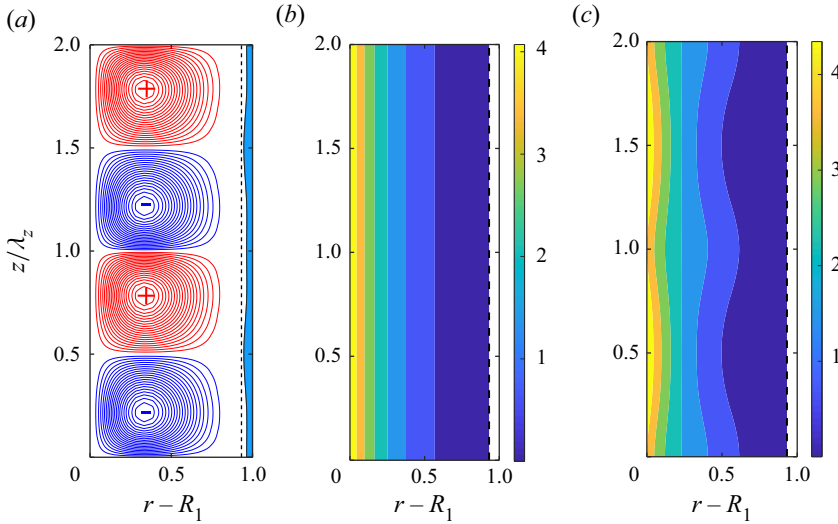


Figure 18. Wide gap, $\eta = 0.4$, with $B = 1$ and stationary outer cylinder. (a) Contours of the stream function $\psi = r\phi$ at $\epsilon = 0.5 \times 10^{-2}$: + indicates clockwise rotation, – indicates anticlockwise rotation. The dashed line indicates the position of the yield surface at critical conditions. (b) Contours of the second invariant $\dot{\gamma}$ of the strain rate tensor $\dot{\boldsymbol{\gamma}}$ at the onset of Taylor vortices, $\epsilon = 0$. (c) Contours of $\dot{\gamma}$ at $\epsilon = 0.5 \times 10^{-2}$.

At the onset of Taylor vortices ($\epsilon = 0$), $\dot{\gamma} = \dot{\gamma}_b(r)$ decreases monotonically from the inner wall to the yield surface represented by a dashed line. At $\epsilon = 0.5 \times 10^{-2}$, in the outward radial flow region, i.e. at approximately $z/\lambda_z = 1$, we have $\dot{\gamma} < \dot{\gamma}_b$ near the inner wall, $\dot{\gamma} = \dot{\gamma}_b$ around the centre of the vortices, and $\dot{\gamma} > \dot{\gamma}_b$ at further radial positions. Opposite behaviours are observed in the inward radial flow region, i.e. at approximately $z/\lambda_z = 0.5$ and 1.5.

Actually, an analysis of the different $\dot{\gamma}_{ij}(\mathbf{U}_b + \mathbf{u})$ shows that $\dot{\gamma}$ is dominated by $|\dot{\gamma}_{r\theta}(\mathbf{U}_b + \mathbf{u})|$. In the outward radial flow region, $\dot{\gamma}_{r\theta}(\mathbf{u})$ is positive and maximum at the inner wall ($\dot{\gamma} < \dot{\gamma}_b$); it decreases and vanishes around the centre of the Taylor vortices ($\dot{\gamma} = \dot{\gamma}_b$), and then becomes negative ($\dot{\gamma} > \dot{\gamma}_b$). Of course, in the regions where $\dot{\gamma} > \dot{\gamma}_b$, we have $\mu < \mu_b$ and vice versa.

5.5. Perturbation of the yield surface

For a sufficiently large Bingham number, a static layer forms and adheres to the outer cylinder. Near the onset of the Taylor vortex flow regime, the disturbed yield surface is given by

$$r = R_y + AH_{11}E^1 + \text{c.c.} + |A|^2 \tilde{H}_{02} + A^2 H_{22}E^2 + \text{c.c.} + O(A^3). \quad (5.5)$$

In figure 19, we have represented contours of the stream function (figure 19a), the deformation of the yield surface (figure 19b), and contours of the azimuthal component of the velocity disturbance (figure 19c). The radius ratio is $\eta = 0.4$, the Bingham number is $B = 1$, and the outer cylinder is stationary. In figure 19(b) a zoom is made on the modification of the yield surface. At critical conditions, the yield surface is represented in a dashed line, and its modification near the onset of vortices in continuous lines. On average, over one wavelength and at second order in amplitude, the thickness of the static layer is reduced by $|A|^2 \tilde{H}_{02}$. This reduction is due on the one hand to the increase in Re_1 , i.e. an increase of the speed of the inner cylinder, and on the other hand to the interaction

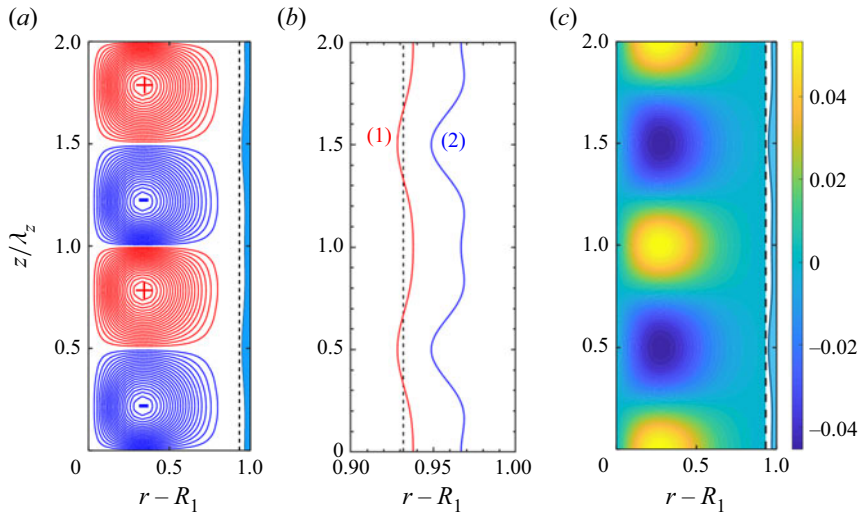


Figure 19. Wide gap, $\eta = 0.4$, with stationary outer cylinder, $B = 1$ and $\epsilon = 0.5 \times 10^{-2}$. (a) Contours of the stream function. The dashed line indicates the position of the yield surface at critical conditions. (b) Zoom on the modification of the yield surface: (1) nonlinear yield stress terms are cancelled artificially; (2) nonlinear yield stress terms are taken into account. (c) Contours of azimuthal velocity perturbations: blue indicates negative azimuthal streaks; yellow indicates positive azimuthal streaks.

of the fundamental mode with its complex conjugate. The numerical results show that less than 7% of the reduction in the static layer thickness is due to the increase in Re_1 , and the remainder is due to the interaction of the fundamental mode with its complex conjugate. More precisely, it is observed that the erosion of the static layer arises mainly from the nonlinear yield stress terms. Indeed, if these nonlinear terms are cancelled artificially, then the erosion will be reduced substantially, as illustrated by curves (1) and (2) in figure 19(b).

Around the average radius of the yield surface $R_y + |A|^2 \tilde{H}_{02}$, a disturbance of small amplitude occurs due to the fundamental mode $AH_{11}E^1 + \text{c.c.}$ and to the second harmonic (interaction of the fundamental with itself) $A^2H_{22}E^2 + \text{c.c.}$. This disturbance of the yield surface shows a ‘hump’ in the region where there is an inward radial flow with a negative azimuthal streak (blue contours in figure 19c) and a ‘trough’ in the region where there is an outward radial flow with a positive azimuthal streak (yellow contours). However, this disturbance around the average radius is quite weak comparatively to the reduction of the width of the plug layer.

Qualitatively similar results are obtained for a higher Bingham number, as shown in figure 20 for $B = 1.4$. However, for the same relative distance to the onset of Taylor vortices, the erosion of the static layer is less pronounced for a larger static layer width.

6. Conclusion

The present work focuses on the first principles in understanding the influence of the yield stress on the stability of a circular Couette flow with respect to a finite-amplitude perturbation. A weakly nonlinear analysis based on the multiple scales method is used as a first approach to take into account nonlinear effects. A Bingham model is used as a typical model of yield stress fluids. A detailed mathematical analysis is provided in the case where the base flow has a plug zone attached to the outer cylinder. The Ginzburg–Landau equation is derived, and the cubic Landau coefficient is determined

Taylor vortices in yield stress fluids

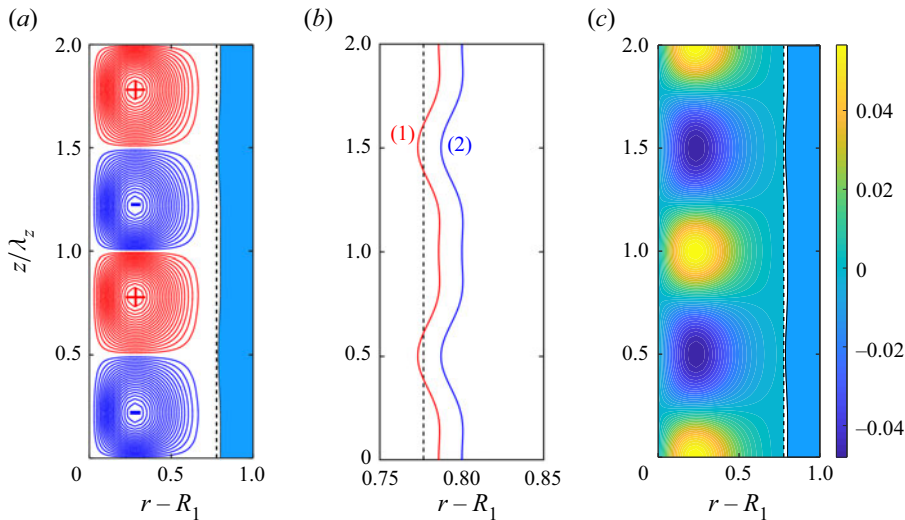


Figure 20. Wide gap, $\eta = 0.4$, with stationary outer cylinder, $B = 1.4$ and $\epsilon = 0.5 \times 10^{-2}$. (a) Contours of the stream function. (b) Zoom on the modification of the yield surface: (1) nonlinear yield stress terms are cancelled artificially; (2) nonlinear yield stress terms are taken into account. (c) Contours of azimuthal velocity perturbations: blue indicates negative azimuthal streaks; yellow indicates positive azimuthal streaks.

for a wide range of Bingham numbers and different radius ratios. The character of the primary bifurcation results from the competition between nonlinear inertia terms that favour a supercritical bifurcation, and nonlinear yield stress terms that favour a subcritical bifurcation. The nonlinear inertia terms are dominant either in the case where the Bingham number is close to zero or in the case where the annular space is sufficiently narrow, i.e. the radius ratio is greater than a limit value η_ℓ , or equivalently, when the yielded fluid domain is sufficiently narrow, $R_1/R_y > \eta_\ell$. However, when $\eta < \eta_\ell$, the nonlinear yield stress terms become dominant and the bifurcation becomes subcritical for a range of B , the extent of which depends on Re_2 and η . To our knowledge, such variations in the nature of the primary bifurcation with B and η were not observed previously in the literature. Concerning the flow structure in the supercritical regime, it is shown that at low values of B , i.e. when the nonlinear inertial terms are dominant, the strength of the vortices decreases slightly with increasing B . However, once the nonlinear yield stress terms that account for the viscosity perturbation start to become significant, the strength of the vortices increases strongly with increasing B . This effect is more pronounced in the presence of a static layer.

Our analysis provides information about the first stages in the evolution of the yield surface when departing from the critical conditions. It is shown that the static layer is reduced due to the increase in the velocity of the inner cylinder and the interaction of the fundamental mode with its complex conjugate involving nonlinear yield stress terms. The contribution of the second effect is much greater than that of the first one. Furthermore, the yield surface is sinusoidally disturbed by the fundamental mode and the second harmonic.

The obvious next step of our analysis is to use a direct numerical simulation to study more deeply the subcritical regime by determining the stable branch and the critical Reynolds number at the onset of vortices. Another point of interest concerns the flow structure and the evolution of the static layer in a strongly nonlinear supercritical regime. Finally, it is worth pointing out the lack of experimental results in the literature.

Supplementary material. Supplementary material is available at <https://doi.org/10.1017/jfm.2023.874>.

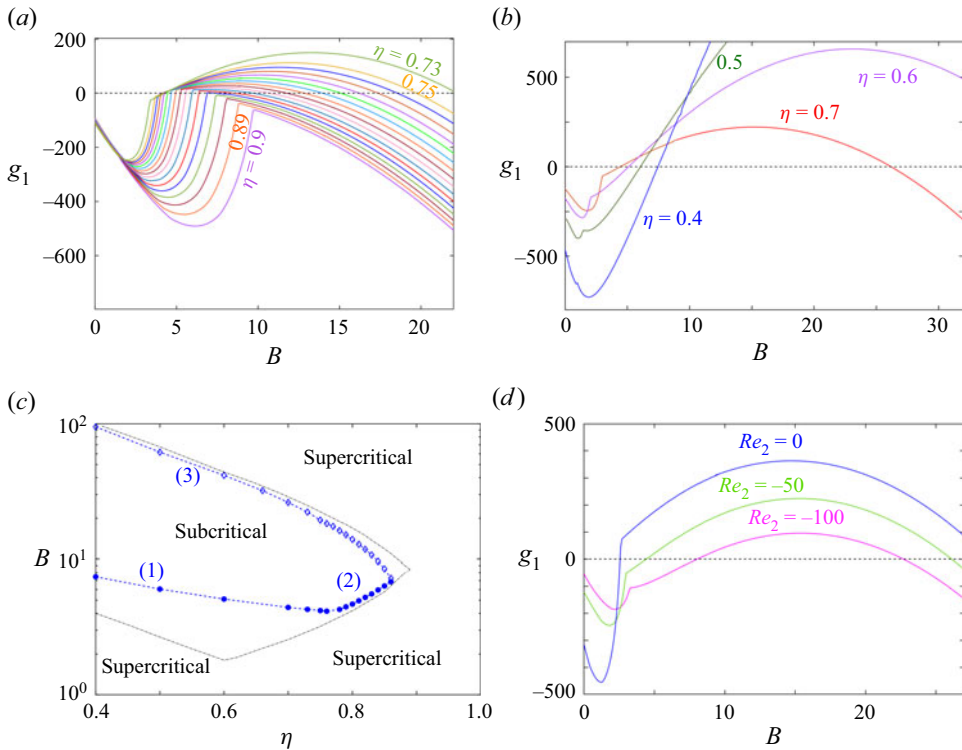


Figure 21. Counter-rotation of the outer cylinder. Variation of the first Landau constant as a function of the Bingham number for different values of the radius ratios at $Re_2 = -50$: (a) from $\eta = 0.9$ until $\eta = 0.75$ by step 0.01, and then $\eta = 0.73$. (b) $\eta = 0.7, 0.6, 0.5, 0.4$. (c) Boundaries of the subcritical domain in the plane (η, B) : (1) and (2) are the lower boundaries, and (3) is the upper boundary. The thin dash-dotted lines are the boundaries of the subcritical domain in the case where the outer cylinder is fixed. (d) Influence of the outer Reynolds number on the first Landau constant for $\eta = 0.7$.

Funding. This research is funded by the Science Committee of the Ministry of Science and Higher Education of the Republic of Kazakhstan (grant no. AP14972680).

Declaration of interests. The authors report no conflict of interest.

Author ORCIDs.

- S. Topayev <https://orcid.org/0000-0003-1860-7911>;
- C. Nouar <https://orcid.org/0000-0002-0457-6694>;
- I. Frigaard <https://orcid.org/0000-0002-0970-240X>.

Author contributions. All authors contributed equally to analysing data and reaching conclusions, and in writing the paper.

Appendix A. Nature of the primary bifurcation

A.1. Counter-rotation of the outer cylinder

We have plotted in figures 21(a,b) the variation of g_1 as a function of B at $Re_2 = -50$, for different radius ratios. Here, the limit radius ratio, from which the bifurcation remains supercritical, is $\eta_\ell = 0.86$. Note in figure 21(c) that the domain of subcriticality is reduced compared to the case where the outer cylinder is fixed. It shrinks further with increasing $|Re_2|$, as depicted in figure 21(d), where we have represented g_1 as a function of B at $\eta = 0.7$ for $Re_2 = 0, -50$ and -100 .

Taylor vortices in yield stress fluids

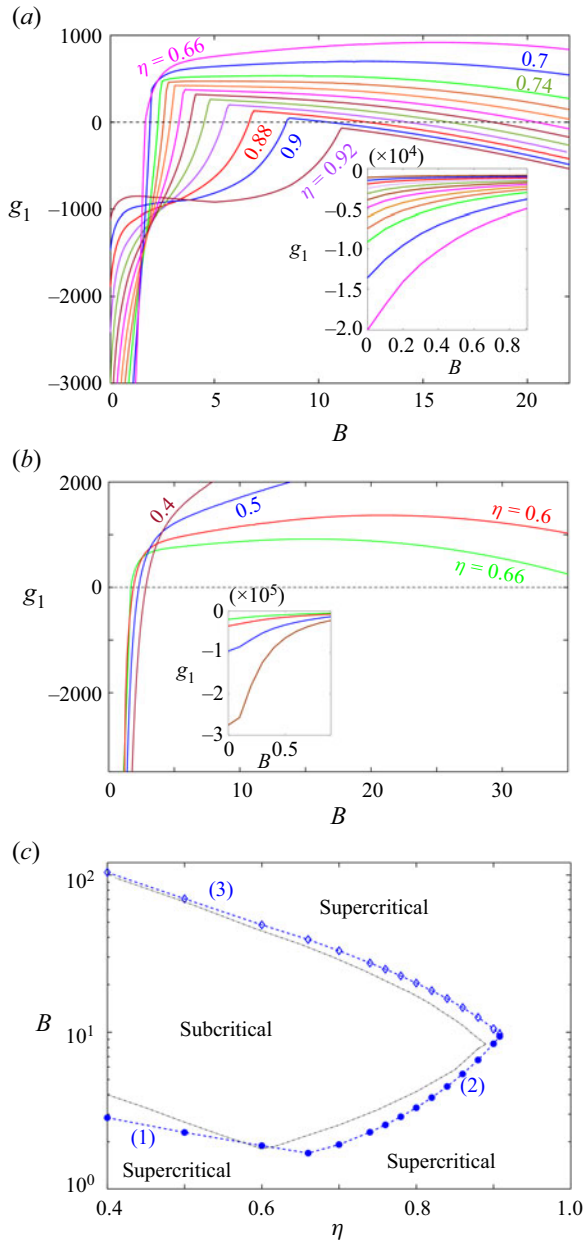


Figure 22. Co-rotation of the outer cylinder. Variation of the first Landau constant as a function of the Bingham number for different values of the radius ratios at $Re_2 = 100$: (a) from $\eta = 0.92$ until $\eta = 0.74$ by step 0.02, and then $\eta = 0.7$ and 0.66 ; (b) $\eta = 0.66, 0.6, 0.5, 0.4$. The inset graphs in (a,b) show the evolution of g_1 at low values of B . (c) Boundaries of the subcritical domain in the plane (η, B) . The thin dash-dotted lines are the boundaries of the subcritical domain when the outer cylinder is fixed.

A.2. Co-rotation of the outer cylinder

The variation of g_1 as a function of B at $Re_2 = 100$ is displayed in figure 22(a) for different radius ratios. Probably the most interesting points that can be noted are as follows. (i) Unlike the previous cases, where $|g_{1I}|$ increases monotonically with B , in the co-rotating case, the variation of $|g_{1I}|$ versus B is non-monotonic, as shown in figure 23. This is a

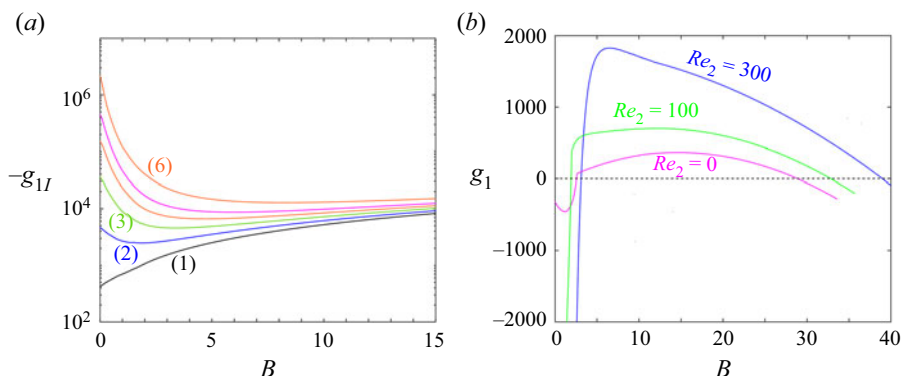


Figure 23. Co-rotation of the outer cylinder. (a) Variation of g_{1l} (contribution of nonlinear inertial terms) as a function of the Bingham number at $\eta = 0.6$ and different values of the outer Reynolds number: (1) $Re_2 = 0$, (2) $Re_2 = 50$, (3) $Re_2 = 100$, (4) $Re_2 = 150$, (5) $Re_2 = 150$, (6) $Re_2 = 300$. (b) Variation of g_1 as a function of the Bingham number at $\eta = 0.7$ and different values of the outer Reynolds number: $Re_2 = 0, 100$ and 300 .

consequence of the non-monotonic variation of Re_{1c} with B (Peng & Zhu 2004; Landry *et al.* 2006). (ii) The numerical results show that the domain of subcritical bifurcation increases with increasing Re_2 , as illustrated by figures 22(c) and 23(b). The radius ratio limit η_ℓ , above which the primary bifurcation remains supercritical, increases slightly with Re_2 . All the results obtained for the variation of η_ℓ as a function of Re_2 , (in co- and counter-rotation) are summarised in figure 8 of the supplementary material.

REFERENCES

- AGBESSI, Y., ALIBENYAHIA, B., NOUAR, C., LEMAITRE, C. & CHOPLIN, L. 2015 Linear stability of Taylor–Couette flow of shear-thinning fluids: modal and non-modal approaches. *J. Fluid Mech.* **776**, 354–389.
- AGWU, O.E., AKPABIO, J.U., EKPENYONG, M.E., INYANG, U.G., ASUQUO, D.E., EYOH, I.J. & ADEOYE, O.S. 2021 A critical review of drilling mud rheological models. *J. Petrol. Sci. Engng* **203**, 108659.
- BALMFORTH, N.J., FRIGAARD, I.A. & OVARLEZ, G. 2014 Yielding to stress: recent developments in viscoplastic fluid mechanics. *Annu. Rev. Fluid Mech.* **46**, 121–146.
- BIRD, R.B., DAI, G.C. & YARUSSO, B.J. 1983 The rheology and flow of viscoplastic materials. *Rev. Chem. Engng* **1**, 1–110.
- BONN, D., DENN, M., BERTHIER, L., DIVOUX, T. & MANNEVILLE, S. 2017 Yield stress materials in soft condensed matter. *Rev. Mod. Phys.* **89** (3), 035005.
- BOUTERAA, M., NOUAR, C., PLAUT, E., MÉTIVIER, C. & KALCK, A. 2015 Weakly nonlinear analysis of Rayleigh–Bénard convection in shear-thinning fluids: nature of the bifurcation and pattern selection. *J. Fluid Mech.* **767**, 696–734.
- CHANDRASEKHAR, S. 1958 The stability of viscous flow between rotating cylinders. *Proc. R. Soc. Lond. A* **246** (1246), 301–311.
- CHANDRASEKHAR, S. 2013 *Hydrodynamic and Hydromagnetic Stability*. Courier Corporation.
- CHEKILA, A., NOUAR, C., PLAUT, E. & NEMDIL, A. 2011 Subcritical bifurcation of shear-thinning plane Poiseuille flows. *J. Fluid Mech.* **686**, 272–298.
- CHEN, C., WAN, Z.-H. & ZHANG, W.-G. 2015 Transient growth in Taylor–Couette flow of a Bingham fluid. *Phys. Rev. E* **91** (4), 043202.
- COUSSOT, P. 1999 Saffman–Taylor instability in yield-stress fluids. *J. Fluid Mech.* **300**, 363–376.
- COUSSOT, P. 2017 Bingham’s heritage. *Rheol. Acta* **56** (3), 163–176.
- DAVEY, A. 1962 The growth of Taylor vortices in flow between rotating cylinders. *J. Fluid Mech.* **14** (3), 336–368.
- DONNELLY, R.J. 1958 Experiments on the stability of viscous flow between rotating cylinders. I. Torque measurements. *Proc. R. Soc. Lond. A* **246** (1246), 312–325.
- FRIGAARD, I. & NOUAR, C. 2003 On three-dimensional linear stability of Poiseuille flow of Bingham fluids. *Phys. Fluids* **15** (10), 2843–2851.

Taylor vortices in yield stress fluids

- FRIGAARD, I.A., HOWISON, S.D. & SOBEY, I.J. 1994 On the stability of Poiseuille flow of a Bingham fluid. *J. Fluid Mech.* **263**, 133–150.
- FRIGAARD, I.A. & NOUAR, C. 2005 On the usage of viscosity regularisation methods for visco-plastic fluid flow computation. *J. Non-Newtonian Fluid Mech.* **127** (1), 1–26.
- FUJIMURA, K. 1989 The equivalence between two perturbation methods in weakly nonlinear stability theory for parallel shear flows. *Proc. R. Soc. Lond. A* **424** (1867), 373–392.
- FUJIMURA, K. 1991 Methods of centre manifold and multiple scales in the theory of weakly nonlinear stability for fluid motions. *Proc. R. Soc. Lond. A* **434** (1892), 719–733.
- GENERALIS, S.C. & FUJIMURA, K. 2009 Range of validity of weakly nonlinear theory in the Rayleigh–Bénard problem. *J. Phys. Soc. Japan* **78** (8), 084401.
- GRAEBEL, W.P. 1961 Stability of a Stokesian fluid in Couette flow. *Phys. Fluids* **4** (3), 362–368.
- HANKS, R.W. 1967 On the flow of Bingham plastic slurries in pipes and between parallel plates. *Soc. Petrol. Engng J.* **7** (04), 342–346.
- HEDSTRÖM, B.O.A. 1952 Flow of plastic materials in pipes. *Ind. Engng Chem. Res.* **44** (3), 651–656.
- HERBERT, T. 1980 Nonlinear stability of parallel flows by high-ordered amplitude expansions. *AIAA J.* **18** (3), 243–248.
- HERBERT, T. 1983 On perturbation methods in nonlinear stability theory. *J. Fluid Mech.* **126**, 167–186.
- JENG, J. & ZHU, K.Q. 2010 Numerical simulation of Taylor–Couette flow of Bingham fluids. *J. Non-Newtonian Fluid Mech.* **165** (19–20), 1161–1170.
- LANDRY, M.P., FRIGAARD, I.A. & MARTINEZ, D.M. 2006 Stability and instability of Taylor–Couette flows of a Bingham fluid. *J. Fluid Mech.* **560**, 321–353.
- MANNEVILLE, P. & CZARNY, O. 2009 Aspect-ratio dependence of transient Taylor vortices close to threshold. *Theor. Comput. Fluid Dyn.* **23**, 15–36.
- MARTINAND, D., SERRE, E. & LUEPTOW, R.M. 2017 Linear and weakly nonlinear analyses of cylindrical Couette flow with axial and radial flows. *J. Fluid Mech.* **824**, 438–476.
- METIVIER, C., NOUAR, C. & BRANCHER, J.P. 2010 Weakly nonlinear dynamics of thermoconvective instability involving viscoplastic fluids. *J. Fluid Mech.* **660**, 316–353.
- NAIMI, M., DEVIENNE, R. & LÉBOUCHÉ, M. 1990 Etude dynamique et thermique de l'écoulement de Couette–Taylor–Poiseuille; cas d'un fluide présentant un seuil d'écoulement. *Intl J. Heat Mass Transfer* **33** (2), 381–391.
- NOUAR, C., KABOUYA, N., DUSEK, J. & MAMOU, M. 2007 Modal and non-modal linear stability of the plane Bingham–Poiseuille flow. *J. Fluid Mech.* **577**, 211–239.
- OVARLEZ, G., RODTS, S., RAGOULLIAUX, A., COUSSOT, P., GOYON, J. & COLIN, A. 2008 Wide-gap Couette flows of dense emulsions: local concentration measurements, and comparison between macroscopic and local constitutive law measurements through magnetic resonance imaging. *Phys. Rev. E* **78** (3), 036307.
- PAPANASTASIOU, T.C. 1987 Flows of materials with yield. *J. Rheol.* **31** (5), 385–404.
- PENG, J. & ZHU, K.-Q. 2004 Linear stability of Bingham fluids in spiral Couette flow. *J. Fluid Mech.* **512**, 21–45.
- RAZZAK, M.A., KHOO, B.C. & LUA, K.B. 2019 Numerical study on wide gap Taylor–Couette flow with flow transition. *Phys. Fluids* **31** (11), 113606.
- SEN, P.K. & VENKATESWARLU, D. 1983 On the stability of plane Poiseuille flow to finite-amplitude disturbances, considering the higher-order Landau coefficients. *J. Fluid Mech.* **133**, 179–206.
- TOPAYEV, S., NOUAR, C., BERNARDIN, D., NEVEU, A. & BAHRANI, S.A. 2019 Taylor-vortex flow in shear-thinning fluids. *Phys. Rev. E* **100** (2), 023117.
- TREFETHEN, L.N. 2000 *Spectral Methods in MATLAB*. SIAM.